Worldwide inference of national methane emissions by inversion of satellite observations with UNFCCC prior estimates

James D. East[1]*, Daniel J. Jacob[1], Dylan Jervis[2], Nicholas Balasus[1], Lucas A. Estrada[1], Sarah E. Hancock[1], Melissa P. Sulprizio[1], John Thomas[1], Xiaolin Wang[1], Zichong Chen[3], Daniel J. Varon[4,5], John Worden[6]

[1] School of Engineering and Applied Science, Harvard University, Cambridge, MA, USA

[2] GHGSat, Inc., Montreal, Canada

[3] Thrust of Carbon Neutrality and Climate Change, Hong Kong University of Science and Technology

[4] Department of Aeronautics and Astronautics, Massachusetts Institute of Technology, Cambridge, MA, USA

[5] Institute for Data, Systems, and Society, Massachusetts Institute of Technology, Cambridge, MA, USA

[6] Jet Propulsion Laboratory, California Institute of Technology, Pasadena, CA, USA

*corresponding author: jeast@g.harvard.edu

Abstract

Meeting climate policy goals to reduce methane emissions under the Paris Agreement and the Global Methane Pledge requires nations to set targets and quantify reductions. Individual countries report emissions by sector to the United Nations Framework Convention on Climate Change (UNFCCC) but there are large uncertainties. Here we optimize 2023 national emissions at up to 25 km grid resolution for 161 countries with a globally consistent open-source framework for inverse analysis of Tropospheric Monitoring Instrument (TROPOMI) satellite observations, using UNFCCC reports for prior estimates together with point source information from GHGSat and other satellites. We find global anthropogenic emissions to be 15% higher than UNFCCC reporting (32% for oil-gas), with national emissions more than 50% higher than reporting for a quarter of the countries. Oil-gas emission intensities vary by two orders of magnitude between countries. Sub-Saharan Africa has the highest livestock emission intensity of any region. Hydroelectric reservoirs, generally not included in UNFCCC reporting, contribute 6% of anthropogenic emissions globally. The framework allows updates for subsequent years, enabling monitoring of emission trends and support for improved reporting.

Introduction

Methane is the second most important anthropogenic greenhouse gas behind CO_2 and has caused 0.6 °C of warming since pre-industrial times[1]. Atmospheric methane concentrations have been rising at an average rate of 0.6% per year for the past decade[2] largely due to increasing emissions[3]. Methane is emitted from multiple anthropogenic sectors including enteric fermentation and manure from livestock, coal mines, oil and natural gas extraction, landfills and wastewater, and rice agriculture, as well as from natural sources, primarily wetlands[4]. It has a relatively short atmospheric lifetime of 9 years, compared to more than 100 years for CO_2. Reducing anthropogenic methane emissions can slow down climate change in the near term while CO_2 reduction technologies are developed and deployed[5–7].

Coordinated international efforts relying on national initiatives aim to advance methane reduction goals. Under the Global Methane Pledge (GMP), 159 signatory nations plus the European Commission have committed to collectively reduce methane emissions by 30% from year 2020 levels by 2030 (https://www.globalmethanepledge.org). The United Nations Framework Convention on Climate Change (UNFCCC) requires all member states to report national emission inventories through National Communications (NCs) and Biennial Update Reports (BURs), culminating in a Global Stocktake and enabling countries to identify Nationally Determined Contributions (NDCs) for reducing methane emissions. The national inventories use bottom-up methods in which emissions for a sector are estimated by multiplying an activity rate (such as oil production) by an emission factor (methane emitted per unit of oil produced), following IPCC procedures at the discretion of each country[8]. However, large uncertainties in these national estimates undermine confidence in the NDCs and in the efficacy of collective action to reduce methane emissions[9,10]. UNFCCC reports may also lag by several years and up to more than a decade, varying between countries. There is a need for a global system to evaluate and guide improvement in national emission inventories using common, consistent, and near-real-time data.

Satellite observations of atmospheric methane can provide such a global system to evaluate national emission inventories. The TROPOMI satellite instrument launched in October 2017 provides global daily observations at 5.5×7 km^2 nadir pixel resolution[11]. GHGSat and other high-resolution instruments can detect point sources worldwide from targeted observations of atmospheric plumes[12]. Emissions can be inferred from these satellite observations using knowledge of atmospheric transport and mature inverse methods[13,14]. This has been done for point sources[15,16] and for individual regions[17–19]. But global inversions have so far

been limited to coarse resolution (hundreds of km) because of computational limitations, compromising the ability to separate emissions by country and even more by sector[20–23].

Here, we present a globally consistent system for estimating methane emissions in all countries of the world with up to 25-km grid resolution by inversion of TROPOMI observations and including point source information from GHGSat. This is done by tiling the world's land masses with eight regional inversions [24], thus relaxing computing requirements, giving better control of boundary conditions, and avoiding effects of errors on the chemical loss. TROPOMI observations are from the blended TROPOMI+GOSAT product of Balasus et al.[25] that corrects TROPOMI artifacts using the more precise but much sparser Greenhouse Gases Observing Satellite (GOSAT) satellite observations. The inversions use the UNFCCC reports from individual countries, spatially allocated following bottom-up inventories, as prior emission estimates so that results can be directly interpreted as corrections to these estimates. Prior emissions for the few countries not reporting to the UNFCCC are estimated using IPCC Tier 1 methods. We use the open-source, user-friendly, cloud-based Integrated Methane Inversion (IMI) version 2.0[26] in all our calculations for transparency, allowing stakeholders to reproduce our results and carry out their own calculations. We apply our system to quantify 2023 emissions for each country and sector, and discuss implications for mitigating methane emissions and for using inverse estimates to aid reporting. Results provide up-to-date observational constraints on emissions from all countries. Our system is set up to allow updates for individual years and thus monitor emission trends.

Results

We estimate emissions at up to 25-km grid resolution for 161 countries with Bayesian analytical inversions of TROPOMI observations of dry column methane mole fractions (XCH_4) using IMI 2.0[26]. The inversion computes optimized (posterior) gridded emissions using error-weighted information from TROPOMI observations and prior emission estimates. Prior anthropogenic emission estimates are from the latest UNFCCC reports for each country, allocated on the 25-km grid using spatial distributions from the Global Fuel Exploitation Inventory (GFEI) v3 and Emissions Database for Global Atmospheric Research (EDGAR) v8 inventories[27,28] and a gridded GHGSat inventory of point sources[29]. Emissions from hydroelectric reservoirs, not included in UNFCCC reports, are added with the ResME inventory[30]. Prior wetland estimates are monthly fluxes at 0.5° resolution from the Lund Potsdam Jena Earth Observation Simulator (LPJ-EOSIM) driven by MERRA-2 meteorology[31]. Atmospheric transport is simulated with the GEOS-Chem

version 14.4.1 chemical transport model at 25-km resolution (https://doi.org/10.5281/zenodo.12584192). We tile the world with eight regional inversions, shown in Fig. 1, encompassing 99.8% of global anthropogenic emissions according to EDGARv8[27]. Boundary conditions are from a global GEOS-Chem simulation bias-corrected to match TROPOMI+GOSAT XCH_4[26]. We optimize emissions at 25-km resolution where the satellite provides high information content and cluster regions with lower information content while respecting national boundaries. Our baseline inversion assumes log-normal error probability density functions (PDFs) for prior emission estimates with a geometric standard deviation of 2.0, and we construct an inversion ensemble varying inversion parameters to characterize the errors on posterior emissions. The sensitivity of the inversion results to the TROPOMI observations (ability to depart from the prior estimate) is measured by the trace of the averaging kernel matrix. The inversions improve the fit to TROPOMI observations in all regions (Fig. S1; Table S2) and better reproduce methane concentrations versus independent surface observations (Fig. S2). The inversions can resolve emissions from all individual countries except small countries with weak emissions, as shown by analysis of posterior error correlation matrices (Figs. S3-S10). They can also distinguish between major emission sectors (Figs. S3-S10) except for landfills and wastewater treatment, which we combine as waste. Optimization of the methane sink from oxidation by OH is effectively accounted for by correction of boundary conditions. Further details are in the Methods section.

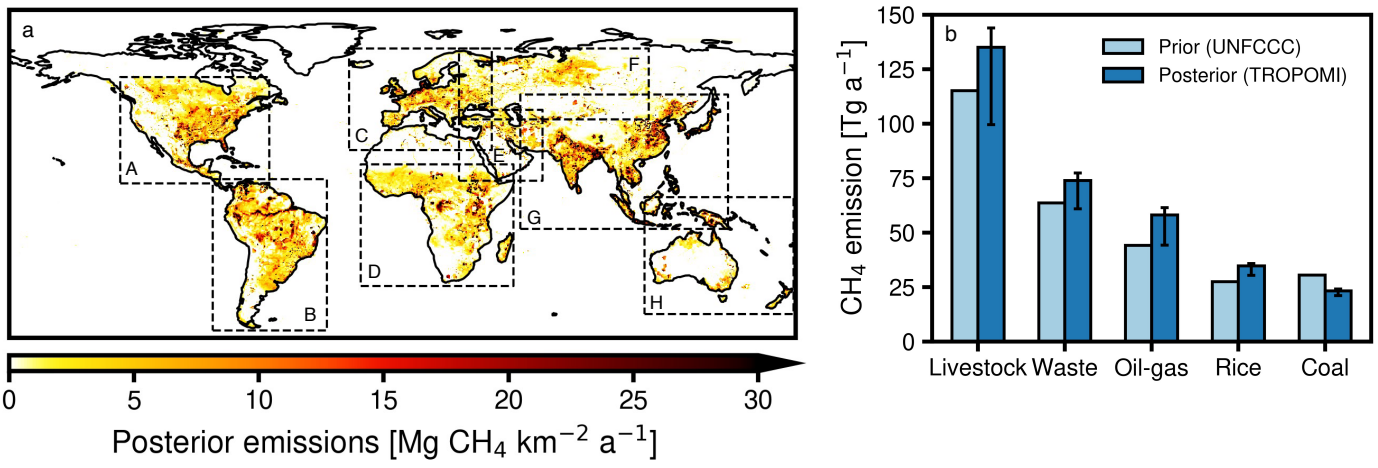

Fig. 1 | Global methane emissions in 2023 estimated by inverse analysis using TROPOMI observations and UNFCCC prior estimates. (a) Posterior emissions from eight regional inversions. Dashed lines show the regional inversion domains. **(b)** Global emissions for major anthropogenic sectors, with error bars from the inversion ensemble.

Global and national emission estimates in comparison to UNFCCC reports

Our global posterior emission estimate for 2023 is 598 (475 – 625) Tg a^{-1}, where parentheses indicate the range from the inversion ensemble. This is higher than the prior estimate of 536 Tg a^{-1} and is consistent with the Global Carbon Project (GCP) top-down estimate for 2023 of 608 (581–627) Tg a^{-1} [32]. Posterior anthropogenic emissions are 375 (299 – 392) Tg a^{-1}, 15% larger than prior emissions (326 Tg a^{-1}). They include 313 (247 – 328) Tg a^{-1} from UNFCCC-reporting countries for livestock, waste, oil-gas, coal, and rice, 13 (10 – 13) Tg a^{-1} from countries not reporting to the UNFCCC (most importantly 9 (8 – 9) Tg a^{-1} from Pakistan), 24 (19 – 25) Tg a^{-1} from hydroelectric reservoirs, and 26 (21 – 28) Tg a^{-1} from minor anthropogenic sources not consistently included in UNFCCC reports including combustion for power generation, combustion for manufacturing, aviation, shipping, rail, road transportation, energy for buildings, chemical production, and iron and steel production. Posterior emissions also include 188 (147-196) Tg a^{-1} from wetlands which aligns with the GCP top-down estimate of 175 (151–229) Tg a^{-1}. The regional distribution of wetland emissions is consistent with global coarse scale TROPOMI inversions for 2023[33]. Fig. 1 shows posterior emissions compared to the UNFCCC prior emissions for global sectors. Posterior emissions include 135 (100 – 144) Tg a^{-1} from livestock (17% higher than UNFCCC totals for the best estimate), 74 (61 – 77) Tg a^{-1} from waste (16% higher), 58 (44 – 61) Tg a^{-1} from oil-gas (32% higher), 35 (31 – 36) Tg from rice (26% higher), and 23 (21 – 24) Tg a^{-1} from coal (24% lower).

Fig. 2 shows our posterior anthropogenic emission estimates for 161 individual countries and the differences with UNFCCC reports for the latest available years. UNFCCC and posterior emissions by sector for each country are in Table S1. We find that national emissions are more than 50% larger than UNFCCC reports in a quarter of all countries and at least 23% smaller in a quarter of all countries. The largest absolute changes are increases in the U.S., Venezuela, India, and Turkmenistan, and decreases in Russia and the Democratic Republic of the Congo. Nations in Africa account for 5 of the top 10 relative increases with factors of 3.4, 3.0, and 1.7 increases in Malawi, Kenya, and Chad, respectively. The Democratic Republic of the Congo (-65%) is an exception that, along with the United Arab Emirates (-63%), has the largest relative decrease among all countries with anthropogenic emissions of at least 0.5 Tg a^{-1}. Venezuela and Turkmenistan increase by factors of 2.5 and 3.2 to 9.0 (4.7 – 9.6) Tg a^{-1} and 7.2 (4.2 – 7.7) Tg a^{-1}, respectively, driven

primarily by oil-gas emissions. Many UNFCCC reports from non-Annex I countries predate 2023, but report age (Fig. S11) plays no role in the match between prior and posterior anthropogenic emissions.

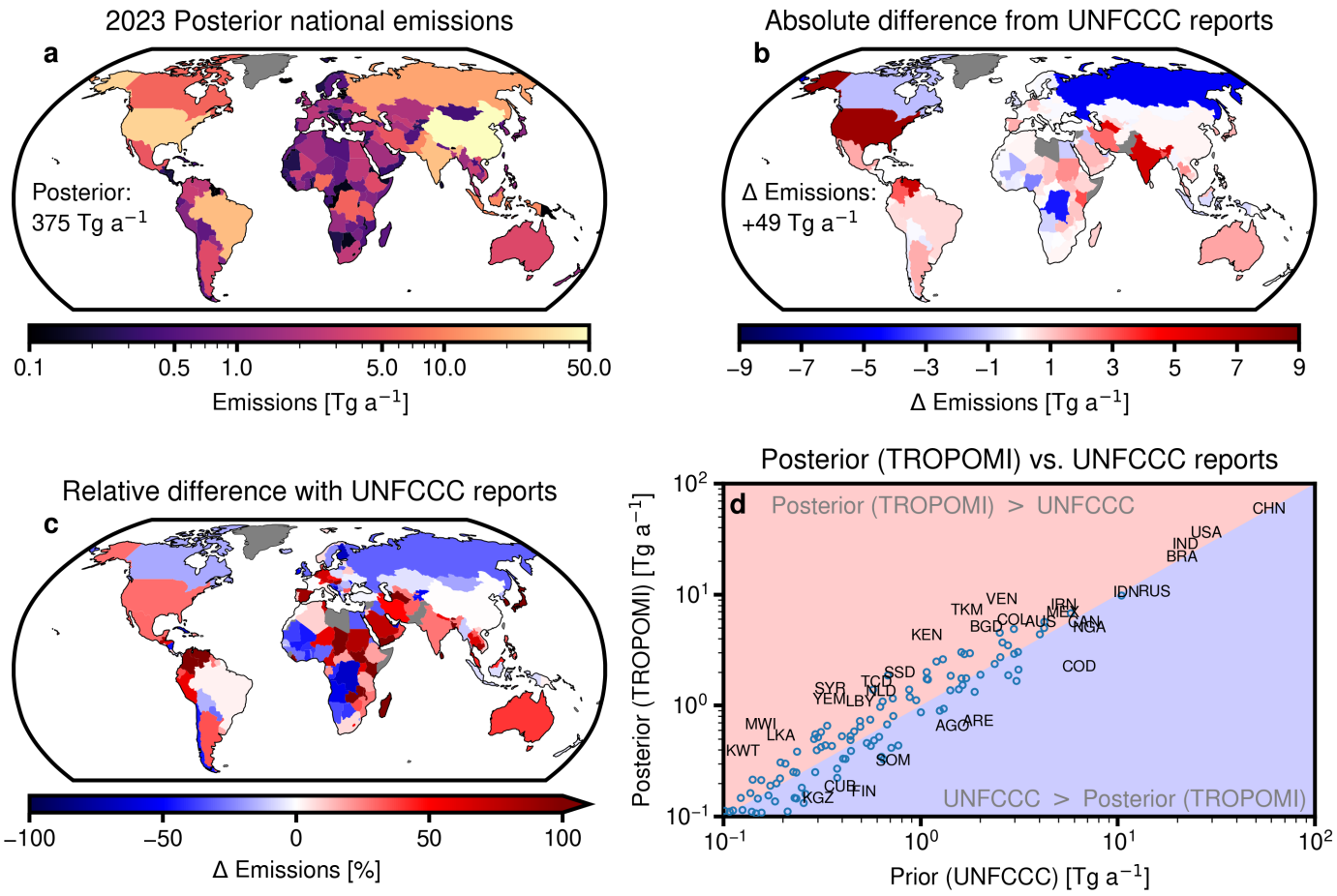

Fig. 2 | Anthropogenic methane emissions from TROPOMI inversions and comparison to UNFCCC reports for individual countries. (a) Posterior 2023 anthropogenic emissions from our baseline TROPOMI inversion. **(b)** and **(c)** Absolute and relative differences from UNFCCC reports. Countries in gray do not report to the UNFCCC. **(d)** Comparison of UNFCCC reports and best posterior estimate for all countries with national emissions greater than 0.1 Tg a^{-1}. Select data points are given as country ISO abbreviations (Table S1), with data at text midpoint. The most recent emissions from the UNFCCC GHG data interface (https://di.unfccc.int/detailed_data_by_party) are used for all countries outside South America and Africa, where the most recently available national communications (NCs) and biennial update reports (BURs) are used. Emissions for all countries and sectors and country abbreviations are given in Table S1.

Fig. 3 shows the top 15 emitting countries from our TROPOMI inversion and the breakdown of anthropogenic emissions by sector. China (59 (49 – 60) Tg a^{-1}), the U.S. (36 (31 – 37) Tg a^{-1}), India (28 (24 – 29) Tg a^{-1}), and Brazil (22 (15 – 23) Tg a^{-1}) account for 39% of global anthropogenic emissions. Additional

contributions from individual countries flatten out so that the top 15 countries account for 61% of global emissions. Among the countries in Fig. 3, the largest corrections from the inversion are in the US (+8.0 Tg a^{-1}), India (+6.0 Tg a^{-1}), Venezuela (+6.4 Tg a^{-1}) and Turkmenistan (+5.4 Tg a^{-1}), and the largest decreases are in Russia (-4.8 Tg a^{-1}) and Indonesia (-0.7 Tg a^{-1}). In the U.S., increases are mainly from oil-gas (13.2 (10.5 – 13.8) Tg a^{-1} posterior, up from 8.5 Tg a^{-1}) and livestock (11.8 (10.6 – 12.2) Tg a^{-1} posterior, up from 9.1 Tg a^{-1}). In China, decreases to coal (14.0 (13.1 – 14.6) Tg a^{-1} posterior, down from 21.2 Tg a^{-1}) offset oil-gas and waste increases. We find that large relative increases are associated with oil-gas emissions, particularly in Venezuela and Turkmenistan where the oil-gas sector is 4.8 and 3.8 times larger, respectively, than UNFCCC prior estimates, along with additional increases from livestock in both countries. In Russia, decreases are spread across sectors, while oil-gas emissions are similar to their UNFCCC report. However, the inversion ensemble shows particularly large uncertainty in our results over Russia because of sparse TROPOMI observations at high latitudes. As a result, we cannot rule out an emissions increase in Russia.

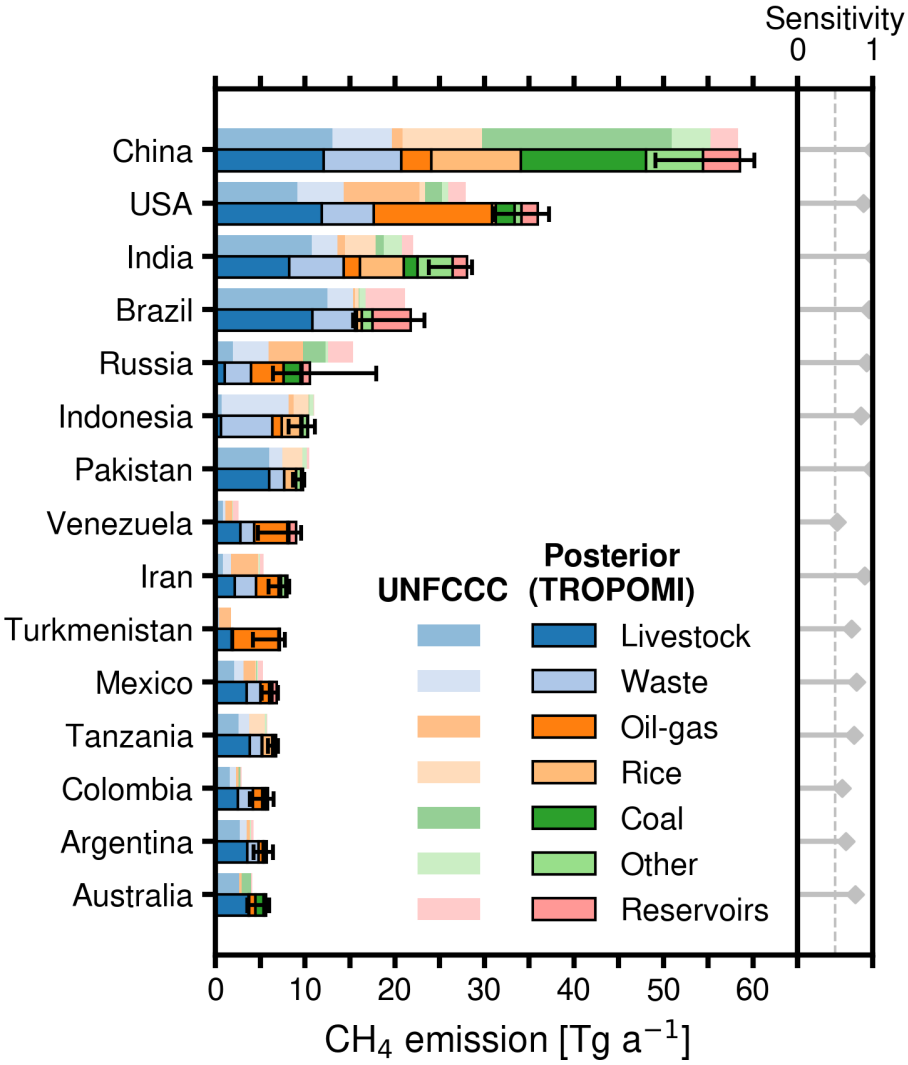

Fig. 3 | National anthropogenic methane emissions from the 15 highest-emitting countries in 2023. Best posterior estimates from the TROPOMI inversion, with error ranges from the inversion ensemble, are compared to the UNFCCC reports including for individual sectors. Also shown is the sensitivity of the inverse estimate to TROPOMI satellite observations as obtained from the trace of the averaging kernel matrix (see Methods).

Sectoral emissions and intensities for individual countries

Fig. 4 shows posterior emissions and emission intensities by sector from our TROPOMI inversion for the top ten emitting countries in each sector, along with the corresponding values from the UNFCCC reports. Emission intensities are computed by dividing posterior emissions by activity levels associated with each sector as defined below.

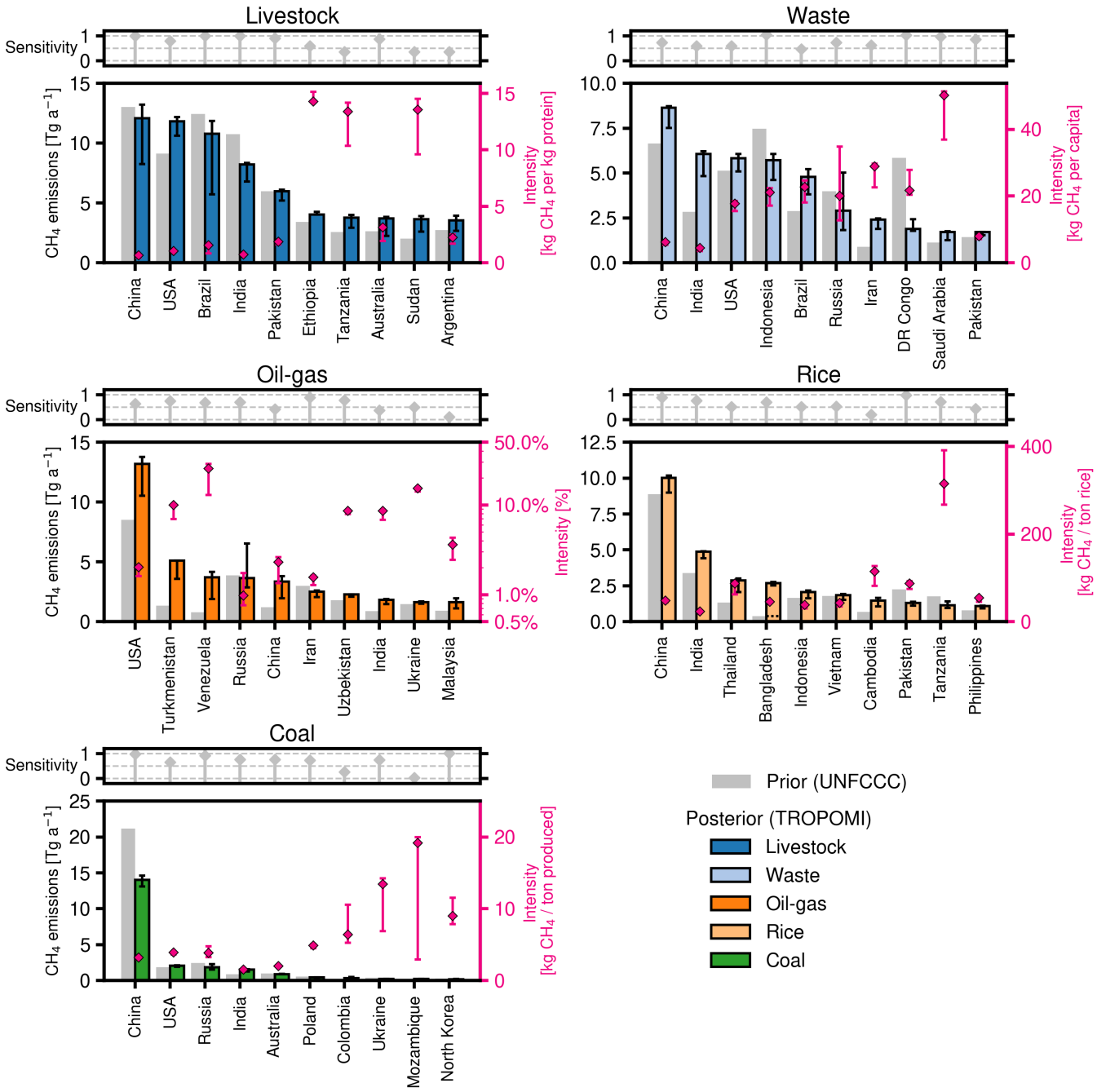

Fig. 4 | National methane emissions and intensities from different sectors. Best posterior estimates from our TROPOMI inversion for 2023 (with ranges from the inversion ensemble) are compared to UNFCCC reports. Intensities are computed from the posterior emissions and activity levels. Gray markers show averaging kernel sensitivities. Country level meat and milk production from major protein-producing livestock are from FAOSTAT (https://www.fao.org/faostat) and the protein content of meat and milk is from FAO[34]. Oil-gas intensity is defined as total oil-gas emissions per unit of gas production, with production data from U.S. Energy Information Administration (EIA) worldwide statistics on dry natural gas production for 2023 (https://www.eia.gov/international/) and assuming 90% methane content of natural gas[24,35]. It

represents the fraction of methane emitted rather than used for fuel, including methane emitted from oil extraction operations. Rice production in 2023 is from FAOSTAT. Coal production for 2023 is from the U.S. EIA (https://www.eia.gov/international/). Dashed line for Bangladesh rice represents posterior emission if its UNFCCC report is used for sectoral allocation.

Livestock

China, the U.S., Brazil, and India are the top emitters from the livestock sector. Worldwide, most of the change to UNFCCC reports comes from lower emitting countries, with a +2.9 Tg a^{-1} net change for the top 10 countries and a +17.0 Tg a^{-1} net change for remaining countries. The largest increases are in East Africa where Kenya, Sudan, and Tanzania total +5.5 Tg a^{-1} over UNFCCC reports, and in the Middle East, particularly Turkmenistan and Iran. In East Africa, the discrepancy may be driven by recent increases in the number of livestock[33,36] that would not be reflected in UNFCCC reports that are on average a decade old. In Brazil, we find a decrease from the UNFCCC report (-1.6 Tg a^{-1}), in line with joint TROPOMI and GOSAT based estimates[37], and a joint inversion of surface and GOSAT observations[21].

We estimate the methane intensity of livestock as emissions per unit of animal protein (milk and meat) from major protein producing livestock. We use country-level FAOSTAT statistics of meat production for cattle, buffalo, chickens including eggs, goats, mules, pigs, and sheep, and milk production for cattle, sheep, and buffalo, along with the protein content for each protein type[34]. Across Sub-Saharan Africa (region D in Fig. 1a), the methane intensity of protein production is 8.0 kg CH_4 per kg protein, compared to 1.1 and 0.8 kg CH_4 per kg protein in North America (region A) and South and East Asia (region G), respectively. The difference is due to lower livestock productivity in Sub-Saharan Africa compared to more intensively managed systems in North America and East Asia[38]. We find a global methane intensity for protein production of 1.4 kg CH_4 per kg protein, closely matching bottom-up estimates of 1.3 kg CH_4 per kg protein[36] but 40% higher than the FAOSTAT estimate of 1.0 kg CH_4 per kg protein.

Waste

China and India have the highest combined wastewater and landfill emissions, which we report together as waste, but the lowest per-capita intensity. The largest changes from UNFCCC reports come from the Democratic Republic of the Congo (-68%; -4.0 Tg a^{-1}) and India (+117%; +3.3 Tg a^{-1}). In China, rapidly increasing waste incineration rates that surpass other countries may contribute to lower intensity[39], while low per-capita waste production in India relative to other countries leads to lower intensity. Treating wastewater could decrease methane intensity in countries with high intensity and low rates of wastewater treatment, such as Indonesia, the Democratic Republic of the Congo, and Iran, where intensities are >20 kg CH_4 per capita and wastewater treatment rates are <40% [40,41].

Oil-gas

The U.S. is the largest methane emitter from the oil-gas sector at 13.2 (10.5-13.7) Tg a^{-1}. We find large upward corrections to the UNFCCC prior emissions for the U.S. (+4.7 (2.0 – 5.3) Tg a^{-1}), Turkmenistan (+3.8 (2.2 – 3.8) Tg a^{-1}), Venezuela (+2.9 (1.1 – 3.4) Tg a^{-1}), and China (+2.2 (0.8 – 2.6) Tg a^{-1}). This underestimate of U.S. emissions has been widely reported[35,42–45]. In China, the increase over its 2014 UNFCCC report may be due in part to recent growth in China's oil-gas emissions[46], and has been found by other inversions[24,47,48]. In Venezuela, large increases from oil-gas emissions over their UNFCCC report are expected[17,37]. Our finding of increases in Turkmenistan oil-gas emissions provides further evidence for larger than reported oil-gas methane from the country[24,49].

In Russia, we find a posterior estimate of 3.6 (2.9 – 6.5) Tg a^{-1}, in line with Russia's UNFCCC report of 3.9 Tg a^{-1}, but again with large uncertainty. Other inversions find larger totals (8-11 Tg a^{-1})[9,22,24,48], which may reflect their use of higher prior estimates. Our posterior estimates in the arctic and subarctic where TROPOMI observation density is limited may be affected by the correction to northern boundary conditions. For Russian emissions we include in our inversion ensemble an additional member with no boundary condition optimization, and consider the results (6.5 Tg a^{-1}) an upper bound on emissions. Spatial overlap with wetlands could also cause uncertainty in Russian oil-gas emissions, but here the effects are minimized by our use of point source observations from GHGSat in the state vector construction.

Fig. 5 shows total oil-gas methane emissions per unit of natural gas production (methane intensity) for the 40 top natural gas producing countries, along with total natural gas production and oil-gas sector CH_4 emissions. Production and intensity are based on U.S. Energy Information Administration (EIA) worldwide statistics on

dry natural gas production for 2023, and assuming 90% methane content of natural gas[24,35]. Intensity represents the fraction of methane emitted rather than used for fuel, including methane emitted from oil extraction operations.We find that 5 countries meet the Oil and Gas Climate Initiative (OGCI) 0.2% methane intensity target, and among those Norway and Qatar are the largest producers. If all countries were to follow suit, then emissions from the oil-gas sector would drop by 81% to 11.0 Tg a^{-1} and become minimal relative to other sectors. We find intensities of 10% or greater from Venezuela (25 (13-29)%, uncertainty from the inversion ensemble range), Ukraine (15 (14-16)%), Colombia (15 (6-16)%), and Turkmenistan (10 (7-10)%), and lower intensities from the largest producers, which include China (2.3 (1.3-2.6)%), the U.S. (2.0 (1.6-2.1)%), Iran (1.6 (1.3-1.6)%), Canada (1.2 (1.1-1.2)%), and Russia (1.0 (0.8-1.7)%). High intensity from Venezuela matches that of Nathan et al.[17] for 2020 using TROPOMI, attributed in part to decreasing production.

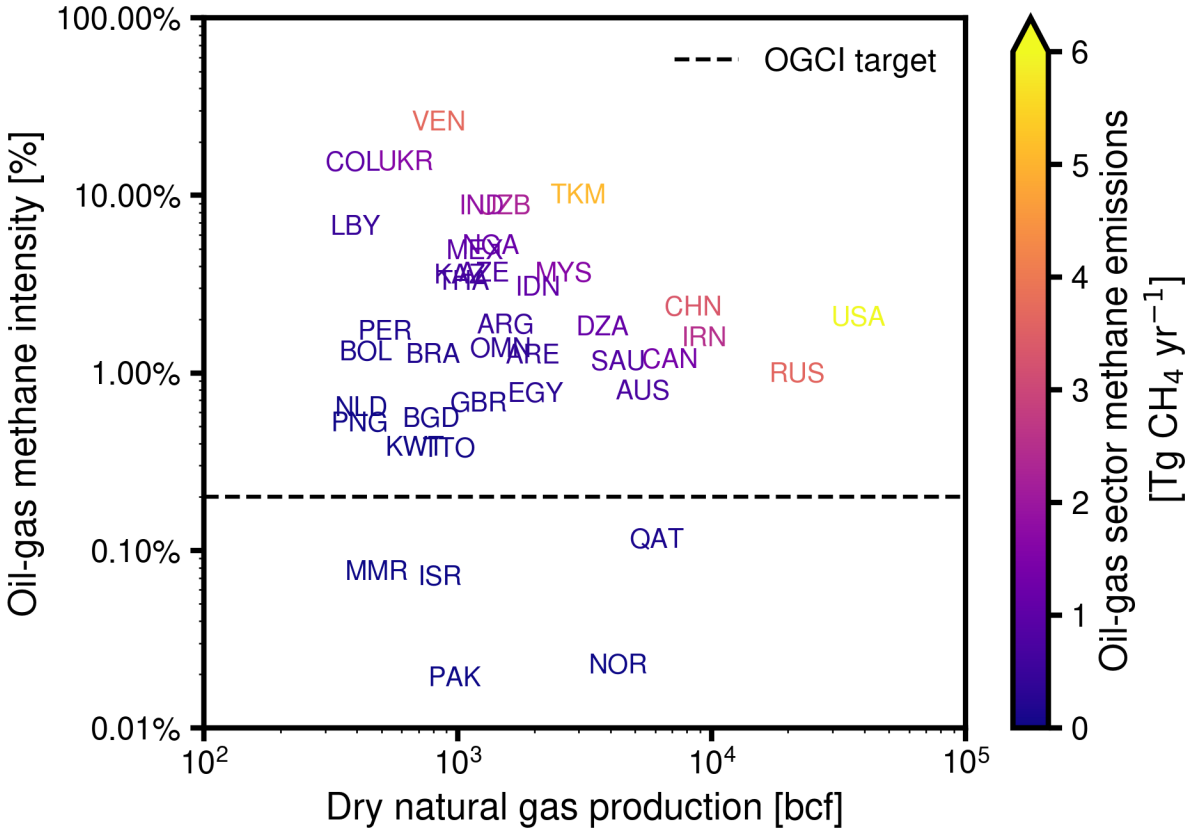

Fig. 5 | Methane intensity for oil-gas sector emissions, dry natural gas production, and oil-gas sector emissions for the 40 top natural gas producing nations. Production data are from U.S. Energy Information Administration (EIA) worldwide statistics on dry natural gas production for 2023 (https://www.eia.gov/international/), and assuming 90% methane content of natural gas[24,35]. Country names are ISO country codes (Table S1). Data are at the text midpoint.

Rice

China (10.0 Tg a^{-1}), India (4.9 Tg a^{-1}), Thailand (2.9 Tg a^{-1}), Bangladesh (2.7 Tg a^{-1}), Indonesia (2.1 Tg a^{-1}), and Vietnam (1.9 Tg a^{-1}) dominate methane emissions from rice. Posterior changes to the global rice sector are not large but there are significant changes from individual countries' reports. Most notable is Bangladesh, which increases by a factor of 7 from its 0.4 Tg UNFCCC report when we use Global Rice Paddy Inventory (GRPI)[50] totals for sectoral allocation. Thailand, India, China, and Cambodia each increase by 0.8 Tg or more, while Pakistan's emissions are 0.9 Tg lower than reports. Our estimate of global methane intensity from rice, 44 kg of methane emitted per ton of rice produced based on FAOSTAT country level statistics, is close to the 51 kg CH_4 per ton of rice reported in the GRPI inventory.

Our estimate for China's rice emissions is larger than its UNFCCC report (8.9 Tg a^{-1}) and GRPI (8.2 Tg a^{-1}) and matches other studies[19]. We find enhanced emissions over the Sanjiang Plain in the northeast, confirming recent growth in rice production and emissions from that region[51]. Among African nations, total emissions are 2.6 Tg a^{-1}, matching a bottom-up estimate which identifies a growing contribution of African rice to global methane emissions[52]. Large rice methane intensity in Tanzania may be due to increasing adoption of higher yield growing methods not reflected in FAOSTAT estimates. Although India's total rice production is similar to that of China, and its harvested area is over 60% larger (48 Mha versus 29 Mha)[53], its emissions of 4.9 (4.4 – 4.9) Tg a^{-1} are 51% lower. Substantially lower emissions factors in India (0.95 kg CH_4 ha^{-1} d^{-1} versus 2.41 kg CH_4 ha^{-1} d^{-1} for China) due to a heavier reliance on rainfed lowland harvesting in India[54] and a shorter rice growing season[50] both contribute to lower rice emissions from India than China.

In Bangladesh, the UNFCCC rice total is low (0.4 Tg a^{-1}) despite the country's status as the world's third largest rice producer. Both rice and wetland prior emissions are uniformly distributed throughout the country [55] and as a result the inversion cannot reallocate emissions to rice from wetlands if we rely on prior fractions in the posterior sectoral breakdown; posterior rice emissions remain locked in at their unrealistically low levels. We ameliorate this by using GRPI emissions for sectoral allocation in Bangladesh (posterior estimate using its UNFCCC report as prior is marked with a dashed line in Fig. 4) and note that this highlights the critical need for high-quality UNFCCC estimates.

Coal

Global coal mine methane emissions are dominated by emissions from China, which accounts for 60% of global coal emissions and 50% of global coal production. We find an annual total of 14.0 Tg a^{-1} in China, down from their UNFCCC estimate of 21.2 Tg a^{-1} with the decrease coming primarily from the Shanxi region and in line with other inversions[19,24,47,48]. The decrease aligns with an ongoing emissions trend driven by a national shift in coal production to surface mines that have lower emissions, countered in our inversion by a minor increase in southern China where abandoned mines continue to emit[56].

Among other coal producing countries and comparing to UNFCCC reports, we find a 0.6 Tg a^{-1} decrease in Russia, a 0.6 Tg a^{-1} increase from India, and negligible changes to U.S. coal emissions. Our inversion is unable to increase the low coal emissions reported to the UNFCCC by Indonesia, despite its status as the second largest coal producer globally, due to low satellite observation density over the region caused by ocean surfaces and extensive cloud cover[24].

Information content from the satellite observations

Averaging kernel sensitivities reported in Figs. 3 and 4 reveal the extent to which the satellite observations inform the posterior estimate. All of the top 15 countries (Fig. 3) have sensitivities greater than 0.5, meaning the posterior estimate is more sensitive to the true emission via the satellite observations than to the prior. Overall, emissions from countries with sensitivities of at least 0.5 represent 89% of posterior anthropogenic emissions. Among individual sectors within countries, sensitivities are high but with exceptions. For example, sensitivities for coal in Mozambique, livestock in Sudan, Argentina, and Tanzania, rice in Cambodia and the Philippines, and oil-gas in China, India, and Malaysia are less than 0.5 due to difficulty of observation (cloudiness, dark surfaces) and relatively low emissions.

Discussion

Our inversions of TROPOMI satellite observations provide information to guide improvement in the bottom-up estimates used as prior estimates. National agencies can use these results to identify sectors where their emission estimates are too low or too high and track progress towards NDCs. In turn, improved bottom-up

inventories can improve the inversions because the prior estimates play an essential role in regularizing the solution; the satellite observations are too sparse otherwise, especially at high latitudes and in regions with excessive cloudiness. In this work, the anomalously low UNFCCC reports for rice emissions in Bangladesh and coal emissions in Indonesia challenge the ability of the inversion to optimize these emissions. We were able to achieve a correction in Bangladesh where satellite observations are dense and an alternative bottom-up rice emission inventory was available, but we were not able to correct Indonesia where observations are sparse. New satellite observation capabilities have the potential to improve inverse emissions estimates; for example, employing higher spatial resolution or intelligent pointing shows promise for providing increased observation density[57,58]. In addition, prior information on spatial and temporal variability of emissions is critical for the inversion because large errors in the spatial distribution of prior emissions propagate to bias in the inversion even when averaging kernel sensitivities are high[59]. National emissions reported to the UNFCCC generally lack spatial and temporal information, so we use alternative inventories to provide that information, but these inventories may not be consistent with the UNFCCC estimates. Incorporating spatial and temporal information with inventory reporting would assist the inversions and improve the sectoral attribution of inversion results[60].

Improved characterization of the spatial and seasonal distribution of wetland emissions, along with their interannual variability, is critical for attribution of anthropogenic emissions in inversions. Current wetland emission inventories have large uncertainties[61,62] and there is extensive spatial overlap of wetland and anthropogenic emissions, for example for oil-gas in Canada and Nigeria, for livestock in South America and Africa, and for rice in Bangladesh and Southeast Asia. Seasonal knowledge of wetland emissions would provide a lever for separating them from anthropogenic emissions in the inversion. New observation products such as the CYGNSS inundation data could be useful for this purpose[63].

In summary, we quantified annual methane emissions at up to 25 km grid resolution for 161 countries by inversion of TROPOMI satellite observations using spatially allocated national UNFCCC reports as prior estimates. We applied the open-source IMI 2.0 to perform the inversion, providing transparency, reproducibility, ease of access to methods and results, and detailed error characterization. Our best posterior estimate of global anthropogenic emissions is 375 (299 – 392) Tg a^{-1}, which is 15% higher than the sum of UNFCCC estimates with upward revisions to livestock (+17%), waste (+16%), oil-gas (+32%), and rice (+26%) and downward revision to coal (-24%). Hydroelectric reservoirs, generally not included in the UNFCCC reports, contribute 6% of our global posterior estimate of anthropogenic emissions. 44 countries

underestimate their emissions by more than 50%. China, the USA, India, and Brazil account together for 39% of global anthropogenic emissions, with the rest widely distributed among other countries. Oil-gas methane intensities for individual countries vary by more than two orders of magnitude, with five countries (notably Norway and Qatar) below the industry target of 0.2%. Sub-Saharan Africa is a major contributor to the global underestimate in livestock emissions, and has a methane intensity per protein produced that is 7 times greater than for North America or East Asia. Our system enables annual emission updates to compare emissions in future years.

Methods

IMI 2.0

We use the Integrated Methane Inversion (IMI) version 2.0[26] for Bayesian optimization of methane emissions worldwide at up to 25-km grid resolution using TROPOMI satellite observations and prior anthropogenic emission estimates from UNFCCC reports. Details on the state vector are given in the state vector construction subsection. The IMI solves the Bayesian cost function analytically to obtain best posterior estimates of gridded emissions (state vector elements) with closed-form error characterization and the ability to readily generate inversion ensembles by varying inversion parameters[64]. The IMI is supported as an open-source, user-friendly tool on the Amazon Web Services (AWS) cloud (https://carboninversion.com/) together with the GEOS-Chem chemical transport model (CTM) that serves as forward model for the inversion. IMI users on the cloud submit their customized inversions by editing a simple configuration file. We apply IMI 2.0 in eight regional inversions, shown in Fig. 1a, with boundary conditions from smoothed TROPOMI observations[26]. The boundary conditions are also optimized in the inversion. The inversion framework and parameters are consistent across the regional inversions, leading to a globally consistent system.

We use the GEOS-Chem chemical transport model version 14.4.1 (https://doi.org/10.5281/zenodo.12584192) at 0.25° × 0.3125° horizontal resolution to construct the Jacobian matrix relating the gridded methane emissions to the concentrations observed by TROPOMI. GEOS-Chem simulates the transport and losses of methane, including chemical loss in the troposphere and stratosphere and monthly soil absorption from

MeMo[65], and is driven by NASA GMAO GEOS Forward Processing (GEOS-FP) assimilated meteorological data[66].

Analytical inversion

We use IMI v2.0 to minimize the Bayesian cost function $J(\boldsymbol{x})$:

$$J(\boldsymbol{x}) = J_A + J_O = (\boldsymbol{x} - \boldsymbol{x_A})^{\mathrm{T}}\mathbf{S_A^{-1}}(\boldsymbol{x} - \boldsymbol{x_A}) + \gamma(\boldsymbol{y} - \mathbf{K}\boldsymbol{x})^{\mathrm{T}}\mathbf{S_O^{-1}}(\boldsymbol{y} - \mathbf{K}\boldsymbol{x}) \quad (1)$$

where $\boldsymbol{x}$ is the emissions state vector also including boundary conditions, $\boldsymbol{x_A}$ is the vector of prior estimates, $\mathbf{S_A}$ is the error covariance matrix of the prior estimate, $\boldsymbol{y}$ is the vector of satellite observations, $\mathbf{K} = \frac{\partial y}{\partial x}$ is the Jacobian matrix which describes the linear sensitivity of $\boldsymbol{y}$ to $\boldsymbol{x}$ and is constructed row-by-row by perturbing individual state vector elements in repeated forward model simulations, $\mathbf{S_O}$ is the observing system error covariance matrix, and $\gamma \in [0, 1]$ is a regularization parameter that is used to prevent overfitting of the solution to observations by accounting for missing off-diagonal structure in $\mathbf{S_O}$. The following subsections describe the different terms.

TROPOMI Observations

We use 2023 observations of atmospheric methane dry-air column mole fractions (XCH_4) from the TROPOMI instrument aboard the sun-synchronous polar-orbiting Sentinel-5 Precursor satellite with an approximate equatorial crossing time of 1:30pm. The TROPOMI XCH_4 operational product from the Space Research Organisation Netherlands (SRON) retrieves in the 2.3 μm band using a full-physics retrieval with 5.5×7 km^2 nadir pixel resolution and daily global coverage[11]. Retrievals are limited to clear-sky scenes. We use the blended TROPOMI+GOSAT XCH_4 product[25] that corrects artifacts in the operational TROPOMI product versions 02.04 – 02.06 using the more precise but sparser GOSAT satellite observations. We exclude coastal pixels, inland water pixels with poor goodness-of-fit in the operational product (SWIR chi-square value > 20000), and glint observations over the oceans which are subject to residual artifacts. The blended TROPOMI+GOSAT product includes only observations for which the operational product has a quality assurance value of 1. Satellite observations are averaged into super-observations on the GEOS-Chem 0.25° × 0.3125° grid for individual orbits, and observational error variances are obtained by the residual error

method accounting for error correlations in the individual observations averaged into super-observations[49]. TROPOMI data are unavailable from 10 to 30 August 2023 due to missing VIIRS cloud data.

UNFCCC reports and prior estimates

Prior anthropogenic emission estimates for individual countries are taken from the countries' UNFCCC reports for livestock, rice, wastewater, landfills, coal, and oil-gas, and are given by sector and country in Table S1. Emissions for the few countries not reporting to the UNFCCC (flagged in Table S1) are estimated using IPCC Tier 1 methods for oil-gas and coal[28] and using EDGARv8 for remaining sectors[27]. For most countries, we used the UNFCCC portal value available from https://di.unfccc.int/detailed_data_by_party. For countries in South America and Africa, UNFCCC totals by sector are based on countries' Biennial Update Reports (BURs) and National Communications (NCs), which may be more recent than the portal values. UNFCCC reports do not include emissions from hydroelectric reservoirs and we add those to the prior national estimates using the ResME bottom-up inventory for individual reservoirs worldwide[30].

UNFCCC inventories are reported as national emission totals for individual sectors, and we distribute them on the 0.25° × 0.3125° grid using bottom-up information from other inventories including the Global Fuel Emissions Inventory (GFEI) version 3[28] for oil-gas and coal, the Global Rice Paddy Inventory (GRPI)[50] for monthly rice, and EDGARv8[27] for other anthropogenic sectors. These spatial distributions are superseded by GHGI Version 2 Express Extension[67] in the U.S., by Scarpelli et al.[68] in Canada, and by Scarpelli et al.[69] in Mexico. Monthly wetland emissions at 0.5°×0.5° resolution are from the Lund-Potsdam-Jena Earth Observation Simulator (LPJ-EOSIM) dynamic global vegetation model driven by MERRA-2 meteorology[31]. Daily biomass burning emissions are from GFED4[70]. Termite emissions are from Fung et al.[71]

Spatial redistribution of fossil fuel emissions using GHGSat

We further redistribute emissions from the oil-gas and coal sectors to account for missing point sources by using global gridded emissions constructed from compiled observations of methane plumes by GHGSat satellite instruments (Fig. 6). The gridded GHGSat product[29] converts instantaneous point-source observations to annual mean emissions on the 0.25° × 0.3125° grid of our inversion using an emissions

persistence model. We incorporate gridded GHGSat emissions in the inversion by adjusting oil-gas and coal emissions according to Eq. 2

$$x^*_{a,i} = \max(G_i, x_{a,i}) \times \frac{\sum_i x_{a,i}}{\sum_i \max(G_i, x_{a,i})} \quad (2)$$

For each gridcell i in a given country, $x^*_{a,i}$ is emission after adjustment by GHGSsat, $x_{a,i}$ is the unadjusted emission from GFEI summing up to UNFCCC national totals[28], and G_i is the gridded GHGSat emission rate. This adjustment is applied separately for oil-gas and coal emissions. The adjusted emissions are then used as prior estimates in the inversion. In this way, locations with missing point sources detected by GHGSat are accounted for in the inversion while the country level totals for oil-gas and coal emissions are maintained.

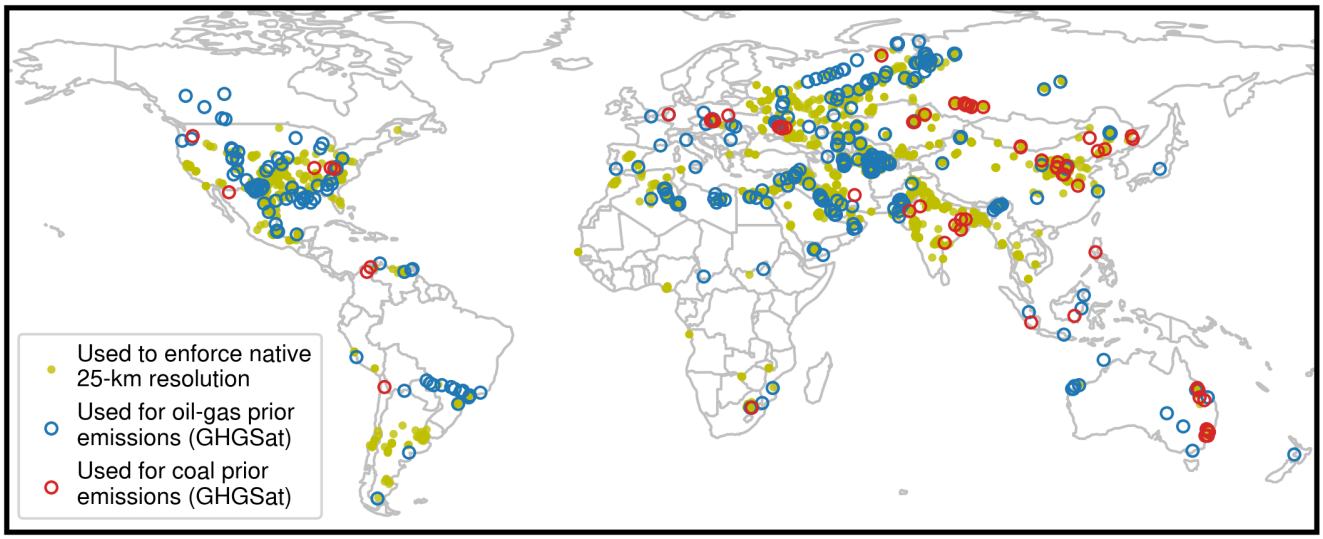

Fig. 6 | Point source information used in the inversions. Open circles are grid cells with prior emissions updated by GHGSat-derived emissions. Yellow closed circles show locations of plumes observed by EMIT, PRISMA, Sentinel-2, Landsat, EnMAP, GOES, and TROPOMI, identifying grid cells to be included in the state vector at the native 25-km native resolution.

State vector construction

The inversions optimize individual elements of the state vector x. For each regional inversion domain, the state vector is composed of emissions from individual and clustered 25-km (0.25° × 0.3125°) GEOS-Chem grid cells over land and offshore, and boundary conditions in the cardinal directions (north, south, west, east)

along the edges of the domains. The maximum resolution (smallest size) of state vector elements is the 0.25° × 0.3125° resolution of the GEOS-Chem forward model, referred to as the native resolution. To reduce the computational cost of the inversion and maximize information content based on prior emissions and TROPOMI observation density, lower-information grid cells are aggregated from the native resolution into clusters using *k*-means[26]. The resolution at which emissions are optimized in the inversion therefore varies, with higher resolution where there are large prior emissions and observation density as determined by averaging kernel sensititivities. Fig. S12 shows the complete size distribution and emissions content of the state vector for an example region (Europe and North Africa). The distribution has a mode of 25-km and and an emission-weighted mean of 93-km (corresponding to a cluster of 14 0.25° × 0.3125° grid cells). In the *k*-means clustering, we impose that clusters do not cross national boundaries in order to avoid ambiguity in attributing emissions to individual countries.

Before clustering the state vector elements, we identify grid cells that are candidates for remaining at native resolution using locations of 8717 methane plumes observed by point source imaging satellite instruments. These include (1) EMIT, PRISMA, Sentinel-2, Landsat, EnMAP, and GOES as reported by the International Methane Emissions Observatory (IMEO) data platform (https://methanedata.unep.org); (2)TROPOMI used for point source detection[72]; and (3) EMIT reported by Carbon Mapper (https://data.carbonmapper.org). Locations of plumes are shown in Fig. 6. Candidate grid cells are all grid cells that contain one or more plumes. Once candidate grid cells are identified, we include at native resolution only those grid cells containing plumes with emission rates above a given threshold after averaging together emission rates of all plumes in the grid cell. For each domain, we test multiple thresholds by building state vectors using thresholds of 0 kg h^{-1} (no threshold; all point source locations used), 2500 kg h^{-1}, and 10000 kg h^{-1}, and comparing the estimated information content of each. The final state vector is constructed by choosing the plume rate emission threshold and *k*-means clustering criteria that yields the highest information content[26]. Grid cells chosen to be at native resolution on the basis of plume locations contain 11% of the global anthropogenic emissions in the posterior estimate. Grid cells in which the prior was adjusted by GHGSat emissions contain 11% of oil-gas and coal emissions.

Uncertainty analysis

The analytical optimization in the IMI returns a closed-form posterior error covariance matrix characterizing the error in the posterior solution but this does not capture uncertainty in inversion parameters, notably the

prior error probability density function (PDF) used to construct the prior error covariance matrix $\mathbf{S_A}$ in Eq (1). . Varying inversion parameters within their expected ranges gives a more conservative estimate of the posterior error (Chen et al., 2022). Here we estimate uncertainty in this manner. We solve for emissions using either normal or lognormal error PDFs for the prior estimates with geometric standard deviations of 1.5, 2.0, or 2.5 for the lognormal error PDFs and standard deviations of 50%, 75%, and 100% for the normal errorPDFs. For each ensemble member, we choose γ so that J_A/n is unity[47]. This results in six unique inversions for each region. We report the emissions for our baseline inversion – lognormal error PDF with geometric standard deviation of 2 – and use other ensemble members to define the posterior uncertainty range. The baseline inversion is chosen as the one with a global emission total that best matches recent estimates[32,33,73]

In the North Asia regional inversion domain (domain F in Fig. 1), emissions are strongly correlated with the inversion's correction to the boundary condition at the northern edge. Along that boundary, there is low observation density, particularly in boreal winter[24], potentially introducing bias into the boundary condition correction and emission results. We therefore include an additional inversion ensemble member in this region with the boundary condition optimization turned off, to test the sensitivity of our results to the boundary correction. Results from this additional inversion are included in the posterior uncertainty range for Russia and discussed in the text.

Attributing emissions to individual countries and sectors

To quantify the total emissions and related information content for individual countries and sectors, we create summation matrices $\boldsymbol{W_n}$, $\boldsymbol{W_c}$, $\boldsymbol{W_s}$, and $\boldsymbol{W_{cs}}$ to produce reduced state vectors and averaging kernel matrices for individual sectors and for individual countries in each inversion, following Chen et al.[47] $\boldsymbol{W_n}$ is a $(p \times n)$ matrix where the rows are the p native resolution GEOS-Chem grid cells, and the columns are the n individual state vector elements. $\boldsymbol{W_c}$ is a $(c \times p)$ matrix of binary values where rows are the c countries in the inversion and columns are the p model grid cells. $\boldsymbol{W_s}$ is a $(s \times p)$ matrix where rows are s emissions sectors and columns are p model grid cells, and values are the annual emissions for each sector in each gridcell. $\boldsymbol{W_{cs}}$ is a $(cs \times p)$ matrix where rows are s emissions sectors in c countries and columns are p model grid cells. We then calculate weighting matrices for countries and sectors on the state vector dimension, $\boldsymbol{W} =$

$\boldsymbol{W_i W_n}$ where $\boldsymbol{W_i}$ can be $\boldsymbol{W_c}$, $\boldsymbol{W_s}$, or $\boldsymbol{W_{cs}}$. $\boldsymbol{W}$ is weighted by emissions and normalized so that its rows sum to 1. We then calculate emissions for countries or sectors:

$$\hat{\boldsymbol{x}}_r = \mathbf{W}\hat{\boldsymbol{x}} \tag{3}$$

Where $\hat{\boldsymbol{x}}_{\boldsymbol{r}}$ is the reduced state vector, giving posterior emissions totals per country and per sector. We use prior sectoral fractions on the 0.25°×0.3125° grid for posterior sectoral allocation, meaning we effectively assume that the relative emission correction within a grid cell applies equally to all sectors in that grid cell[22,74], but at 25-km resolution the resulting error is minimized because a single sector is more likely to dominate. We calculate posterior error covariance and averaging kernel matrices for countries or sectors:

$$\mathbf{S}_{\mathrm{r}} = \mathbf{W}\mathbf{S}\mathbf{W}^{\mathrm{T}} \tag{4}$$

$$\mathbf{A}_{\mathrm{r}} = \mathbf{I}_{\mathrm{n}} - \hat{\mathbf{S}}_{\mathrm{r}}\mathbf{S}_{\mathrm{A,r}}^{-1} \tag{5}$$

where $\mathbf{S}$ in Eq. 4 is either $\hat{\mathbf{S}}$ or $\mathbf{S_A}$, and $\mathbf{A_r}$ is the reduced averaging kernel matrix. Diagonal elements of $\mathbf{A_r}$ give the sensitivity, from zero to one, of the solution to the true state for individual sectors and countries. An averaging kernel sensitivity near zero means that the solution is primarily informed by the prior estimate, while a value near one means that the solution is determined by the TROPOMI observations with little sensitivity to the prior estimate.

In some cases, inversion domains overlap. Fig. S13 and Fig. 1a show the inversion domains. To avoid errors due to overlap between different regional inversions, each country's emissions are optimized by a single inversion. For locations where inversion domains overlap, posterior emissions for the country are taken from the primary inversion domain for that country, as shown in Fig. S13.

Evaluation against observations

We evaluate the inversion results against TROPOMI observations and against independent methane observations using the NOAA GLOBALVIEWplus CH4 ObsPack v7.0 database of surface sites

worldwide[75]. Globally, bias against TROPOMI is eliminated using simulations with posterior emissions (prior bias of -1.9 ppb, posterior bias of 0.1 ppb), and RMSE is reduced from 7.7 ppb (prior) to 5.6 ppb (posterior). For the individual regional inversions, RMSE decreases in all cases. Mean bias is reduced in four of eight regions (Europe and North Africa, North Asia, East Asia, and Oceania), and biases in the other regions are small (<1.1 ppb). Details for each region are in Fig. S1 and Table S2. For comparison against surface observations, we sample the model prior and posterior simulations for each region at the locations and times of the observations for all sites more than 4° away from the domain edge, and limited to the 10-16 local time window to avoid the effect of nighttime stratification. Fig. S2 shows the comparison between modeled and observed concentrations and site locations for the 208 sites used in the evaluation. On average globally, annual root mean square error (RMSE) improves by 9 ppb (29 ppb to 20 ppb) and bias improves by 8 ppb (-23 ppb to -15 ppb). RMSE improves in all regions and bias improves in all regions except Oceania, where the model already performs well and change in the bias is small. The bias in simulating surface observations could reflect model error in vertical mixing[76] but also nearby emissions affecting the observations.

Data Availability

All results are freely accessible on an interactive website where results for individual countries can be queried including emissions and the information content at https://johnthomasseas.github.io/TilingTheWorld/ (temporary site for demonstration purposes only during review, URL will change). Table S1 with results for all individual countries can also be directly accessed on figshare (DOI link not yet available). Configuration files are available upon request and can be used to perform inversions on AWS using IMIv2.0. Blended TROPOMI+GOSAT data is available at https://registry.opendata.aws/blended-tropomi-gosat-methane/. Inputs to run GEOS-Chem including emission fields, boundary condition fields, and meteorological fields are available from AWS at https://registry.opendata.aws/geoschem-input-data/.

Code Availability

The IMI code and documentation are available at https://carboninversion.com and the source code is also archived at https://doi.org/10.5281/zenodo.6081933. The GEOS-Chem model code is available at https://doi.org/10.5281/zenodo.12584192.

Acknowledgments

This work was supported in the framework of UNEP's International Methane Emissions Observatory (IMEO). This work was supported by the NASA Carbon Monitoring System (CMS). Portions of this research were carried out at the Jet Propulsion Laboratory, California Institute of Technology, under a contract with the National Aeronautics and Space Administration. John Worden acknowledges support from the NASA Carbon Monitoring System (22-CMS22-0010).

Author Contributions

JDE and DJJ contributed to the study conceptualization. JDE conducted the inversions and analysis and wrote the first draft of the manuscript. DJ provided GHGSat emissions data. JT created website for results. DJJ, DJ, NB, LAE, SEH, MPS, XW, ZC, DJV, and JW contributed to interpretation of results. All authors provided input on the manuscript.

References

1. IPCC. Climate Change 2021: The Physical Science Basis. Contribution of Working Group I to the Sixth Assessment Report of the Intergovernmental Panel on Climate Change. in (ed. Masson-Delmotte, V., P. Zhai, A. Pirani, S.L. Connors, C. Péan, S. Berger, N. Caud, Y. Chen, L. Goldfarb, M.I. Gomis, M. Huang, K. Leitzell, E. Lonnoy, J.B.R. Matthews, T.K. Maycock, T. Waterfield, O. Yelekçi, R. Yu, B. Z.) (Cambridge University Press., 2021).

2. Lan, X., Thoning, K. & Dlugokencky, E. Trends in globally-averaged CH4, N2O, and SF6 determined from NOAA Global Monitoring Laboratory measurements. NOAA GML https://doi.org/10.15138/P8XG-AA10 (2025).

3. Turner, A. J., Frankenberg, C. & Kort, E. A. Interpreting contemporary trends in atmospheric methane. *Proc. Natl. Acad. Sci. U.S.A.* **116**, 2805–2813 (2019).

4. Jackson, R. B. *et al.* Human activities now fuel two-thirds of global methane emissions. *Environ. Res. Lett.* **19**, 101002 (2024).

5. Nisbet, E. G. *et al.* Methane Mitigation: Methods to Reduce Emissions, on the Path to the Paris Agreement. *Reviews of Geophysics* **58**, e2019RG000675 (2020).

6. Ocko, I. B. *et al.* Acting rapidly to deploy readily available methane mitigation measures by sector can immediately slow global warming. *Environ. Res. Lett.* **16**, 054042 (2021).

7. Shindell, D. *et al.* The methane imperative. *Front. Sci.* **2**, 1349770 (2024).

8. IPCC. *2019 Refinement to the 2006 IPCC Guidelines for National Greenhouse Gas Inventories*. https://www.ipcc.ch/report/2019-refinement-to-the-2006-ipcc-guidelines-for-national-greenhouse-gas-inventories/ (2019).

9. Deng, Z. *et al.* Comparing national greenhouse gas budgets reported in UNFCCC inventories against atmospheric inversions. *Earth Syst. Sci. Data* **14**, 1639–1675 (2022).

10. Olczak, M., Piebalgs, A. & Balcombe, P. A global review of methane policies reveals that only 13% of emissions are covered with unclear effectiveness. *One Earth* **6**, 519–535 (2023).

11. Lorente, A. *et al.* Methane retrieved from TROPOMI: improvement of the data product and validation of the first 2 years of measurements. *Atmos. Meas. Tech.* **14**, 665–684 (2021).

12. Jervis, D. *et al.* The GHGSat-D imaging spectrometer. *Atmos. Meas. Tech.* **14**, 2127–2140 (2021).

13. Jacob, D. J. *et al.* Satellite observations of atmospheric methane and their value for quantifying methane emissions. *Atmos. Chem. Phys.* **16**, 14371–14396 (2016).

14. Jacob, D. J. *et al.* Quantifying methane emissions from the global scale down to point sources using satellite observations of atmospheric methane. *Atmos. Chem. Phys.* **22**, 9617–9646 (2022).

15. Irakulis-Loitxate, I. *et al.* Satellite-based survey of extreme methane emissions in the Permian basin. *Sci. Adv.* **7**, eabf4507 (2021).

16. Lauvaux, T. *et al.* Global assessment of oil and gas methane ultra-emitters. *Science* **375**, 557–561 (2022).

17. Nathan, B. *et al.* Assessing methane emissions from collapsing Venezuelan oil production using TROPOMI. *Atmos. Chem. Phys.* **24**, 6845–6863 (2024).

18. Sicsik-Paré, A. *et al.* Can we obtain consistent estimates of the emissions in Europe from three different CH4 TROPOMI products? Preprint at https://doi.org/10.5194/egusphere-2025-2622 (2025).

19. Zhang, Y. *et al.* Observed changes in China's methane emissions linked to policy drivers. *Proc. Natl. Acad. Sci. U.S.A.* **119**, e2202742119 (2022).

20. Feng, L., Palmer, P. I., Parker, R. J., Lunt, M. F. & Bösch, H. Methane emissions are predominantly responsible for record-breaking atmospheric methane growth rates in 2020 and 2021. *Atmos. Chem. Phys.* (2023).

21. Janardanan, R. *et al.* Country-level methane emissions and their sectoral trends during 2009–2020 estimated by high-resolution inversion of GOSAT and surface observations. *Environ. Res. Lett.* **19**, 034007 (2024).

22. Worden, J. R. *et al.* The 2019 methane budget and uncertainties at 1° resolution and each country through Bayesian integration Of GOSAT total column methane data and a priori inventory estimates. *Atmos. Chem. Phys.* **22**, 6811–6841 (2022).

23. Yu, X. *et al.* A high-resolution satellite-based map of global methane emissions reveals missing wetland, fossil fuel, and monsoon sources. *Atmos. Chem. Phys.* **23**, 3325–3346 (2023).

24. Shen, L. *et al.* National quantifications of methane emissions from fuel exploitation using high resolution inversions of satellite observations. *Nat Commun* **14**, 4948 (2023).

25. Balasus, N. *et al.* A blended TROPOMI+GOSAT satellite data product for atmospheric methane using machine learning to correct retrieval biases. *Atmos. Meas. Tech.* **16**, 3787–3807 (2023).

26. Estrada, L. A. *et al.* Integrated Methane Inversion (IMI) 2.0: an improved research and stakeholder tool for monitoring total methane emissions with high resolution worldwide using TROPOMI satellite observations. *Geosci. Model Dev.* **18**, 3311–3330 (2025).

27. Crippa, M. *et al.* Insights into the spatial distribution of global, national, and subnational greenhouse gas emissions in the Emissions Database for Global Atmospheric Research (EDGAR v8.0). *Earth Syst. Sci. Data* **16**, 2811–2830 (2024).

28. Scarpelli, T. R. *et al.* Using new geospatial data and 2020 fossil fuel methane emissions for the Global Fuel Exploitation Inventory (GFEI) v3. Preprint at https://doi.org/10.5194/essd-2024-552 (2025).

29. Jervis, D. *et al.* Global Energy Sector Methane Emissions Estimated by using Facility-Level Satellite Observations. Preprint at https://doi.org/10.31223/X5V15D (2025).

30. Delwiche, K. B. *et al.* Estimating Drivers and Pathways for Hydroelectric Reservoir Methane Emissions Using a New Mechanistic Model. *JGR Biogeosciences* **127**, e2022JG006908 (2022).

31. Zhang, Z. *et al.* Recent intensification of wetland methane feedback. *Nat. Clim. Chang.* **13**, 430–433 (2023).

32. Saunois, M. *et al.* Global Methane Budget 2000–2020. *Earth Syst. Sci. Data* **17**, 1873–1958 (2025).

33. Pendergrass, D. C. *et al.* Trends and seasonality of 2019–2023 global methane emissions inferred from a localized ensemble transform Kalman filter (CHEEREIO v1.3.1) applied to TROPOMI satellite observations. Preprint at https://doi.org/10.5194/egusphere-2025-1554 (2025).

34. FAO. GLEAM model description. Version 3.0. Table 9.1. (2022).

35. Alvarez, R. A. *et al.* Assessment of methane emissions from the U.S. oil and gas supply chain. *Science* **361**, 186–188 (2018).

36. Chang, J. *et al.* The Key Role of Production Efficiency Changes in Livestock Methane Emission Mitigation. *AGU Advances* **2**, e2021AV000391 (2021).

37. Hancock, S. E. *et al.* Satellite quantification of methane emissions from South American countries: a high-resolution inversion of TROPOMI and GOSAT observations. *Atmos. Chem. Phys.* **25**, 797–817 (2025).

38. Herrero, M. *et al.* Biomass use, production, feed efficiencies, and greenhouse gas emissions from global livestock systems. *Proc. Natl. Acad. Sci. U.S.A.* **110**, 20888–20893 (2013).

39. Lu, J.-W., Zhang, S., Hai, J. & Lei, M. Status and perspectives of municipal solid waste incineration in China: A comparison with developed regions. *Waste Management* **69**, 170–186 (2017).

40. De Foy, B., Schauer, J. J., Lorente, A. & Borsdorff, T. Investigating high methane emissions from urban areas detected by TROPOMI and their association with untreated wastewater. *Environ. Res. Lett.* **18**, 044004 (2023).

41. Jones, E. R., Van Vliet, M. T. H., Qadir, M. & Bierkens, M. F. P. Country-level and gridded estimates of wastewater production, collection, treatment and reuse. *Earth Syst. Sci. Data* **13**, 237–254 (2021).

42. Miller, S. M. *et al.* Anthropogenic emissions of methane in the United States. *Proc. Natl. Acad. Sci. U.S.A.* **110**, 20018–20022 (2013).

43. Nesser, H. *et al.* High-resolution US methane emissions inferred from an inversion of 2019 TROPOMI satellite data: contributions from individual states, urban areas, and landfills. *Atmos. Chem. Phys.* **24**, 5069–5091 (2024).

44. Omara, M. *et al.* Constructing a measurement-based spatially explicit inventory of US oil and gas methane emissions (2021). *Earth Syst. Sci. Data* **16**, 3973–3991 (2024).

45. Rutherford, J. S. *et al.* Closing the methane gap in US oil and natural gas production emissions inventories. *Nat Commun* **12**, 4715 (2021).

46. Wang, F. *et al.* Atmospheric observations suggest methane emissions in north-eastern China growing with natural gas use. *Sci Rep* **12**, 18587 (2022).

47. Chen, Z. *et al.* Methane emissions from China: a high-resolution inversion of TROPOMI satellite observations. *Atmos. Chem. Phys.* **22**, 10809–10826 (2022).

48. Tibrewal, K. *et al.* Assessment of methane emissions from oil, gas and coal sectors across inventories and atmospheric inversions. *Commun Earth Environ* **5**, 26 (2024).

49. Chen, Z. *et al.* Satellite quantification of methane emissions and oil–gas methane intensities from individual countries in the Middle East and North Africa: implications for climate action. *Atmos. Chem. Phys.* **23**, 5945–5967 (2023).

50. Chen, Z. *et al.* Global Rice Paddy Inventory (GRPI): A High-Resolution Inventory of Methane Emissions From Rice Agriculture Based on Landsat Satellite Inundation Data. *Earth's Future* **13**, e2024EF005479 (2025).

51. Liang, R. *et al.* Satellite-Based Monitoring of Methane Emissions from China's Rice Hub. *Environ. Sci. Technol.* **58**, 23127–23137 (2024).

52. Chen, Z., Balasus, N., Lin, H., Nesser, H. & Jacob, D. J. African rice cultivation linked to rising methane. *Nat. Clim. Chang.* **14**, 148–151 (2024).

53. FAOSTAT. Crops and livestock products. (2025).

54. Nikolaisen, M. *et al.* Methane emissions from rice paddies globally: A quantitative statistical review of controlling variables and modelling of emission factors. *Journal of Cleaner Production* **409**, 137245 (2023).

55. Peters, C. N., Bennartz, R. & Hornberger, G. M. Satellite-derived methane emissions from inundation in Bangladesh. *JGR Biogeosciences* **122**, 1137–1155 (2017).

56. Gao, J., Guan, C., Zhang, B. & Li, K. Decreasing methane emissions from China's coal mining with rebounded coal production. *Environ. Res. Lett.* **16**, 124037 (2021).

57. Frankenberg, C. *et al.* Data Drought in the Humid Tropics: How to Overcome the Cloud Barrier in Greenhouse Gas Remote Sensing. *Geophysical Research Letters* **51**, e2024GL108791 (2024).

58. Nassar, R. *et al.* Intelligent pointing increases the fraction of cloud-free CO2 and CH4 observations from space. *Front. Remote Sens.* **4**, 1233803 (2023).

59. Yu, X., Millet, D. B. & Henze, D. K. How well can inverse analyses of high-resolution satellite data resolve heterogeneous methane fluxes? Observing system simulation experiments with the GEOS-Chem adjoint model (v35). *Geosci. Model Dev.* **14**, 7775–7793 (2021).

60. Nassar, R. *et al.* Improving the temporal and spatial distribution of CO_2 emissions from global fossil fuel emission data sets. *JGR Atmospheres* **118**, 917–933 (2013).

61. East, J. D. *et al.* Interpreting the Seasonality of Atmospheric Methane. *Geophysical Research Letters* **51**, e2024GL108494 (2024).

62. Zhang, Z. *et al.* Ensemble estimates of global wetland methane emissions over 2000–2020. *Biogeosciences* **22**, 305–321 (2025).

63. Xiong, Y. *et al.* Limited evidence that tropical inundation and precipitation powered the 2020–2022 methane surge. *Commun Earth Environ* **6**, 450 (2025).

64. Varon, D. J. *et al.* Integrated Methane Inversion (IMI 1.0): a user-friendly, cloud-based facility for inferring high-resolution methane emissions from TROPOMI satellite observations. *Geosci. Model Dev.* **15**, 5787–5805 (2022).

65. Murguia-Flores, F., Arndt, S., Ganesan, A. L., Murray-Tortarolo, G. & Hornibrook, E. R. C. Soil Methanotrophy Model (MeMo v1.0): a process-based model to quantify global uptake of atmospheric methane by soil. *Geosci. Model Dev.* **11**, 2009–2032 (2018).

66. Lucchesi, R. *File Specification for GEOS FP (Forward Processing)*. https://gmao.gsfc.nasa.gov/pubs/docs/Lucchesi1203.pdf (2018).

67. Maasakkers, J. D. *et al.* A Gridded Inventory of Annual 2012–2018 U.S. Anthropogenic Methane Emissions. *Environ. Sci. Technol.* **57**, 16276–16288 (2023).

68. Scarpelli, T. R., Jacob, D. J., Moran, M., Reuland, F. & Gordon, D. A gridded inventory of Canada's anthropogenic methane emissions. *Environ. Res. Lett.* **17**, 014007 (2022).

69. Scarpelli, T. R. *et al.* A gridded inventory of anthropogenic methane emissions from Mexico based on Mexico's national inventory of greenhouse gases and compounds. *Environ. Res. Lett.* **15**, 105015 (2020).

70. Van Der Werf, G. R. *et al.* Global fire emissions estimates during 1997–2016. *Earth Syst. Sci. Data* **9**, 697–720 (2017).

71. Fung, I. *et al.* Three-dimensional model synthesis of the global methane cycle. *J. Geophys. Res.* **96**, 13033 (1991).

72. Schuit, B. J. *et al.* Automated detection and monitoring of methane super-emitters using satellite data. *Atmos. Chem. Phys.* **23**, 9071–9098 (2023).

73. He, M. *et al.* Attributing 2019-2024 methane growth using TROPOMI satellite observations. Preprint at https://doi.org/10.22541/essoar.174886142.25607118/v1 (2025).

74. Cusworth, D. H. *et al.* A Bayesian framework for deriving sector-based methane emissions from top-down fluxes. *Commun Earth Environ* **2**, 242 (2021).

75. Schuldt, K. N. *et al.* Multi-laboratory compilation of atmospheric carbon dioxide data for the period 1983-2023; obspack_ch4_1_GLOBALVIEWplus_v7.0_2024-10-29. NOAA Global Monitoring Laboratory https://doi.org/10.25925/20241001 (2024).

76. Yu, K. *et al.* Errors and improvements in the use of archived meteorological data for chemical transport modeling: an analysis using GEOS-Chem v11-01 driven by GEOS-5 meteorology. *Geosci. Model Dev.* **11**, 305–319 (2018).

Supplementary information for **Worldwide inference of national methane emissions by inversion of satellite observations and UNFCCC prior estimates**

James D. East[1]*, Daniel J. Jacob[1], Dylan Jervis[2], Nicholas Balasus[1], Lucas A. Estrada[1], Sarah E. Hancock[1], Melissa P. Sulprizio[1], John Thomas[1], Xiaolin Wang[1], Zichong Chen[3], Daniel J. Varon[4,5], John Worden[6]

[1] School of Engineering and Applied Science, Harvard University, Cambridge, MA, USA
[2] GHGSat, Inc., Montreal, Canada
[3] Thrust of Carbon Neutrality and Climate Change, Hong Kong University of Science and Technology
[4] Department of Aeronautics and Astronautics, Massachusetts Institute of Technology, Cambridge, MA, USA
[5] Institute for Data, Systems, and Society, Massachusetts Institute of Technology, Cambridge, MA, USA
[6] Jet Propulsion Laboratory, California Institute of Technology, Pasadena, CA, USA

*corresponding author: jeast@g.harvard.edu

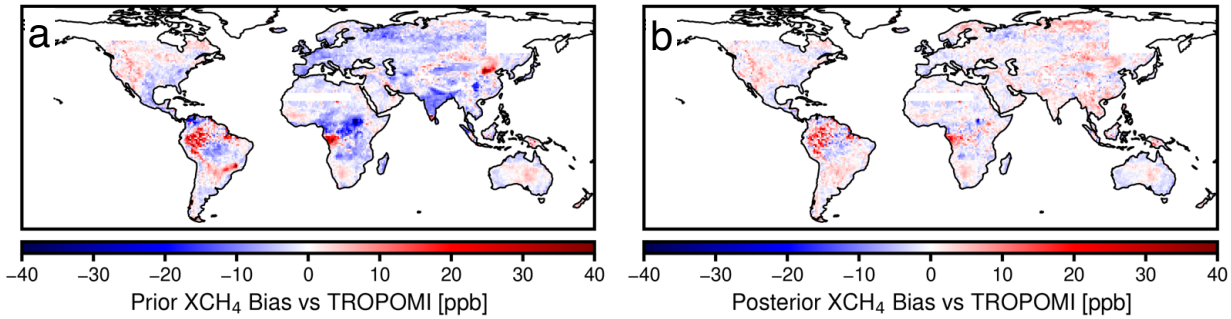

Fig. S1 | GEOS-Chem model bias compared to TROPOMI XCH_4. Maps show the union of all eight regional domains' annual mean bias in GEOS-Chem XCH_4 using **(a)** prior UNFCCC emissions or **(b)** posterior emissions and sampled with the satellite averaging kernel in all cases, versus TROPOMI XCH_4. Maps are coarsened to the 1°×1° scale for visualization only.

Table S2. | RMSE and bias in GEOS-Chem compared to TROPOMI XCH_4 with prior or posterior emissions.

	Prior		Posterior	
Region	**Bias [ppb]**	**RMSE [ppb]**	**Bias [ppb]**	**RMSE [ppb]**
North America	-0.3	11.9	0.5	11.4
South America	-0.4	12.8	0.5	9.7
Europe and North Africa	-1.5	9.1	0.8	8.8
Sub-Saharan Africa	-0.4	9.6	1.1	8.9
Middle East	-0.3	9.2	0.9	8.2
North Asia	-2.7	12.4	0.3	11.6
East Asia	-2.4	14.2	1.2	11.4
Oceania	0.8	6.7	-0.3	6.5

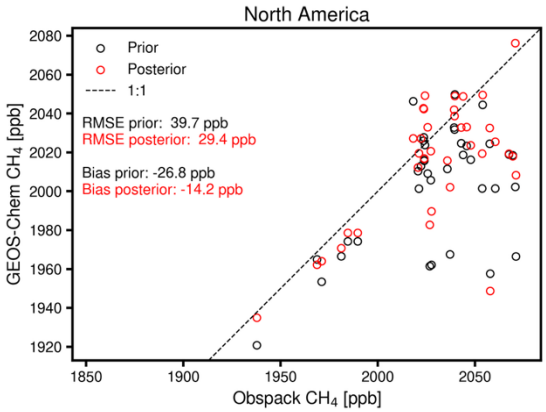
North America
Prior
Posterior
1:1
RMSE prior: 39.7 ppb
RMSE posterior: 29.4 ppb
Bias prior: -26.8 ppb
Bias posterior: -14.2 ppb
GEOS-Chem CH4 [ppb]
Obspack CH4 [ppb]

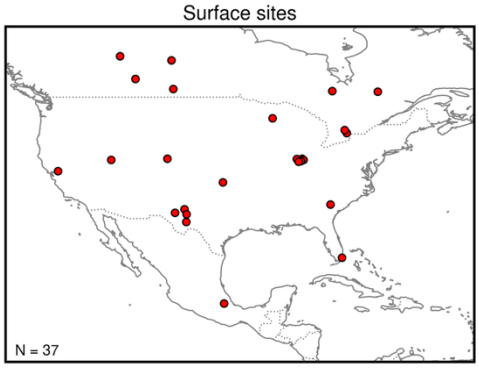
Surface sites
N = 37

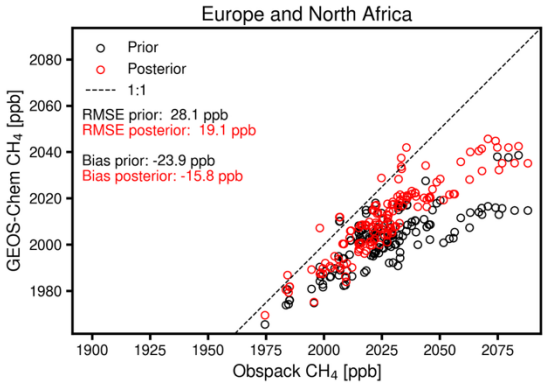
Europe and North Africa
Prior
Posterior
1:1
RMSE prior: 28.1 ppb
RMSE posterior: 19.1 ppb
Bias prior: -23.9 ppb
Bias posterior: -15.8 ppb
GEOS-Chem CH4 [ppb]
Obspack CH4 [ppb]

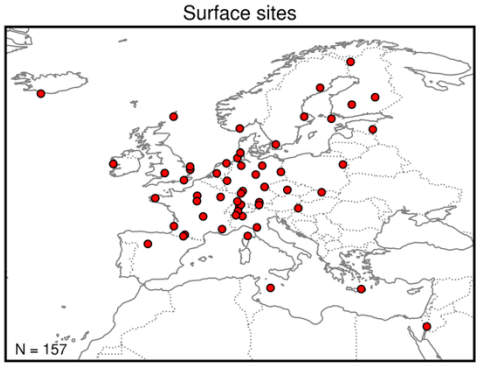
Surface sites
N = 157

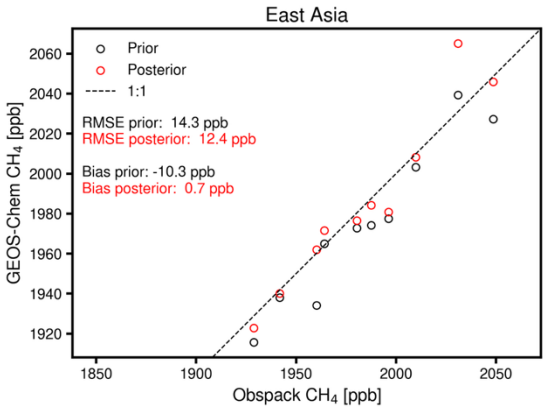
East Asia
Prior
Posterior
1:1
RMSE prior: 14.3 ppb
RMSE posterior: 12.4 ppb
Bias prior: -10.3 ppb
Bias posterior: 0.7 ppb
GEOS-Chem CH4 [ppb]
Obspack CH4 [ppb]

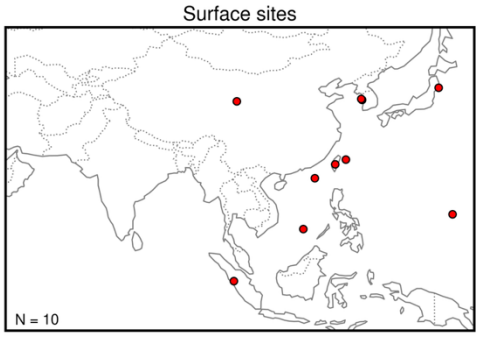
Surface sites
N = 10

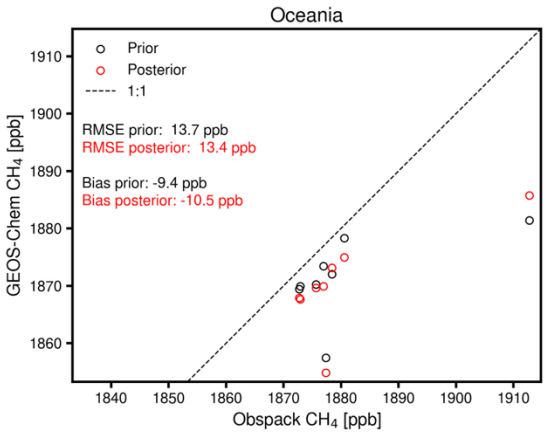
Oceania
Prior
Posterior
1:1
RMSE prior: 13.7 ppb
RMSE posterior: 13.4 ppb
Bias prior: -9.4 ppb
Bias posterior: -10.5 ppb
GEOS-Chem CH4 [ppb]
Obspack CH4 [ppb]

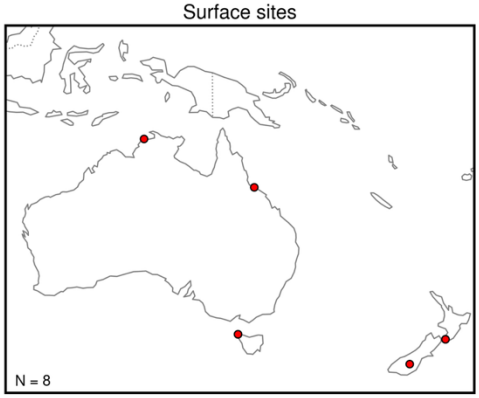
Surface sites
N = 8

Fig. S2 | Evaluation of inversion results with independent surface observations. The figure compares annual average modeled and observed CH4 concentrations from surface flask and in-situ sites in the NOAA GLOBALVIEWplus CH4 ObsPack v7.0 database. Annual mean bias, root mean square errors (RMSE), and site locations for each region are given in the figures. "N" in site maps denotes number of unique annual datasets, some of which are co-located.

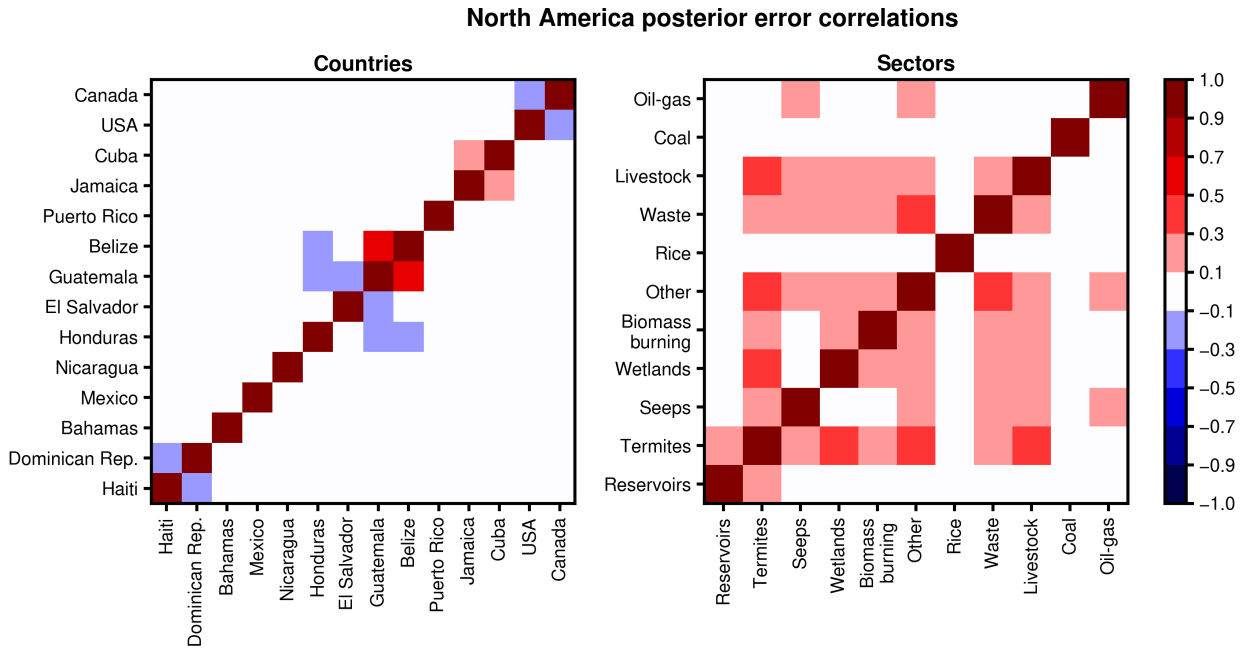

Fig. S3 | Posterior error correlations between individual countries and sectors in North America. Results are for region A in Fig. 1. Posterior error correlation coefficients (r) between posterior estimates of methane emissions from difference sectors and total emissions from countries in the inversion domain for the regional inversion. Error correlations measure the ability of the inversion to separate emissions among individual countries or sectors ($r = \pm 1$: unable to separate; $r = 0$: fully able to separate).

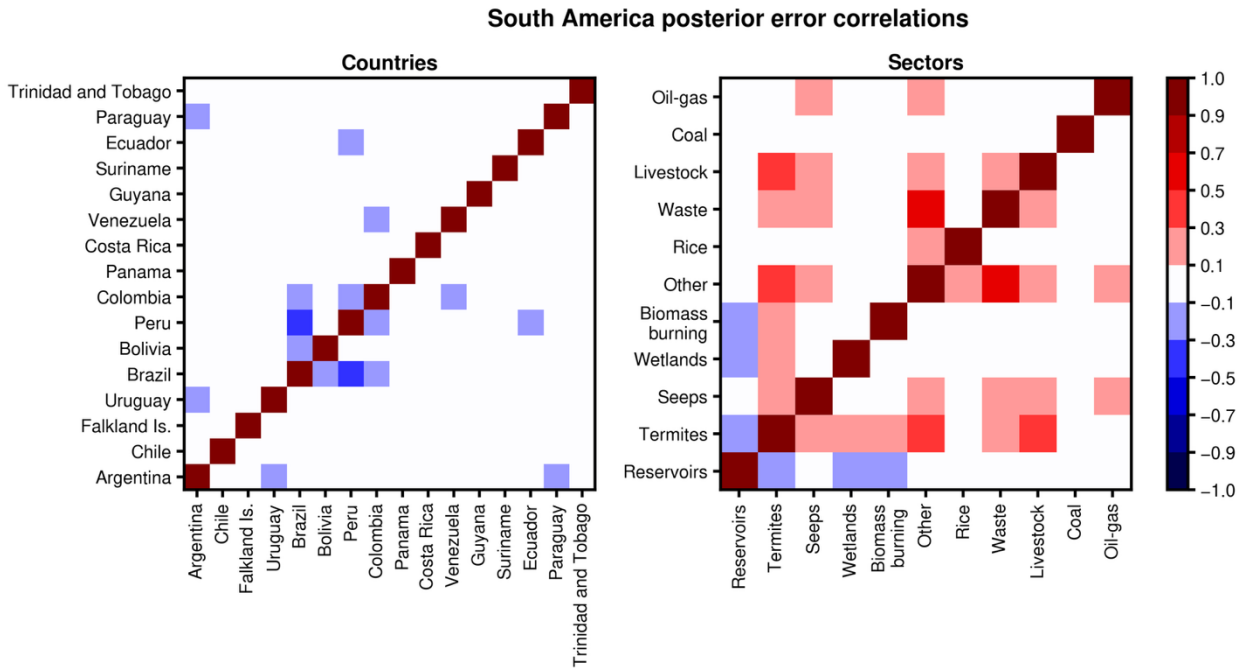

Fig. S4 | Posterior error correlations between individual countries and sectors in South America. As in Fig. S3. Results are for region B in Fig. 1.

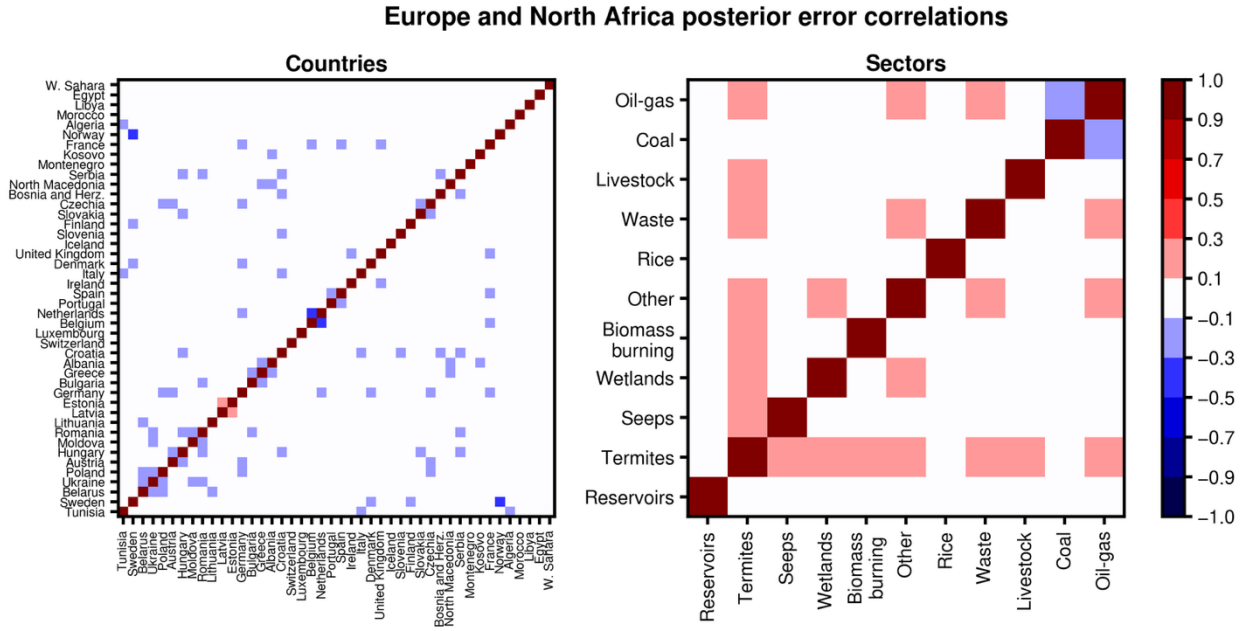

Fig. S5 | Posterior error correlations between individual countries and sectors in Europe and North Africa. As in Fig. S3. Results are for region C in Fig. 1.

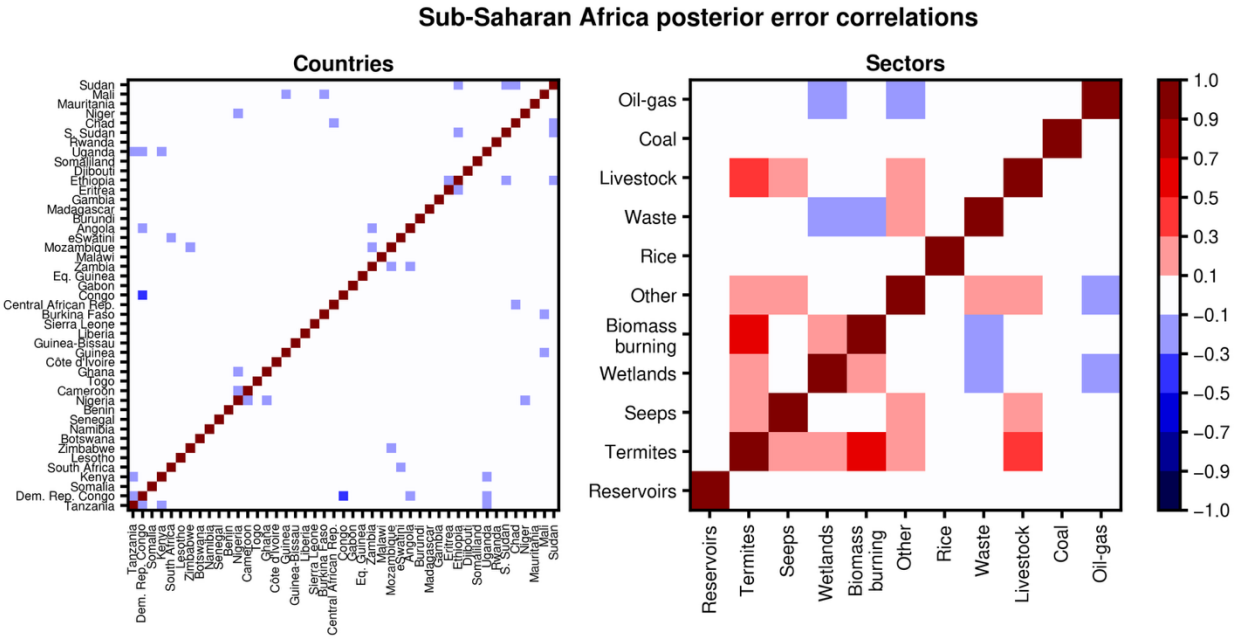

Fig. S6 | Posterior error correlations between individual countries and sectors in Sub-Saharan Africa. As in Fig. S3. Results are for region D in Fig. 1.

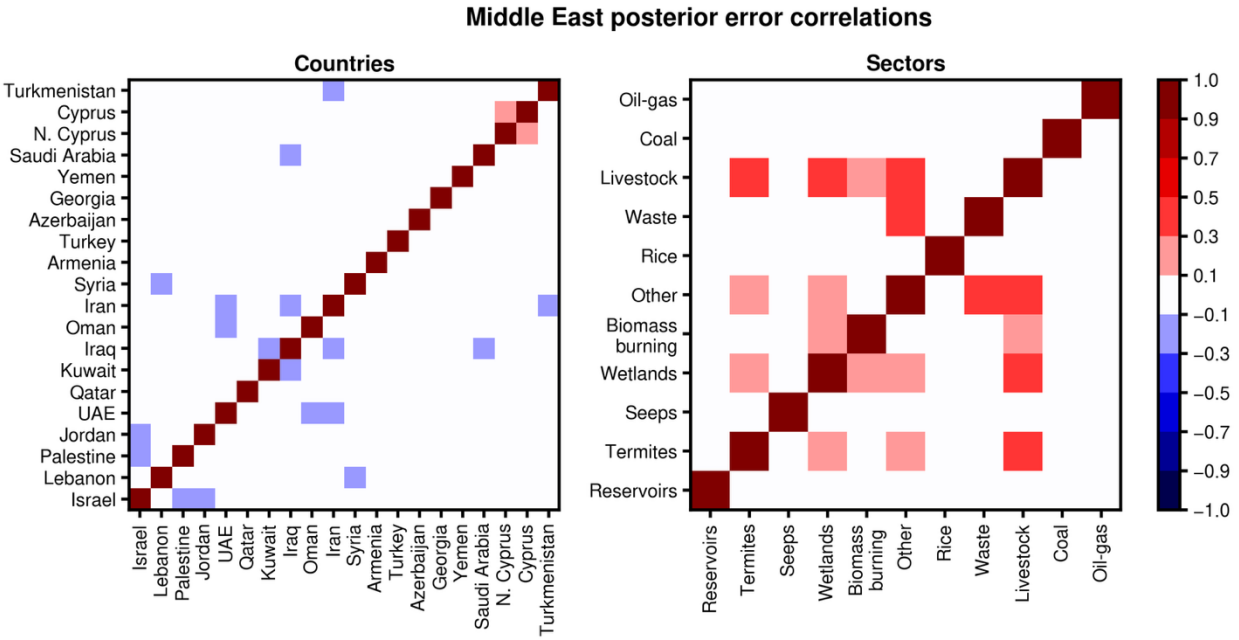

Fig. S7 | Posterior error correlations between individual countries and sectors in the Middle East. As in Fig. S3. Results are for region E in Fig. 1.

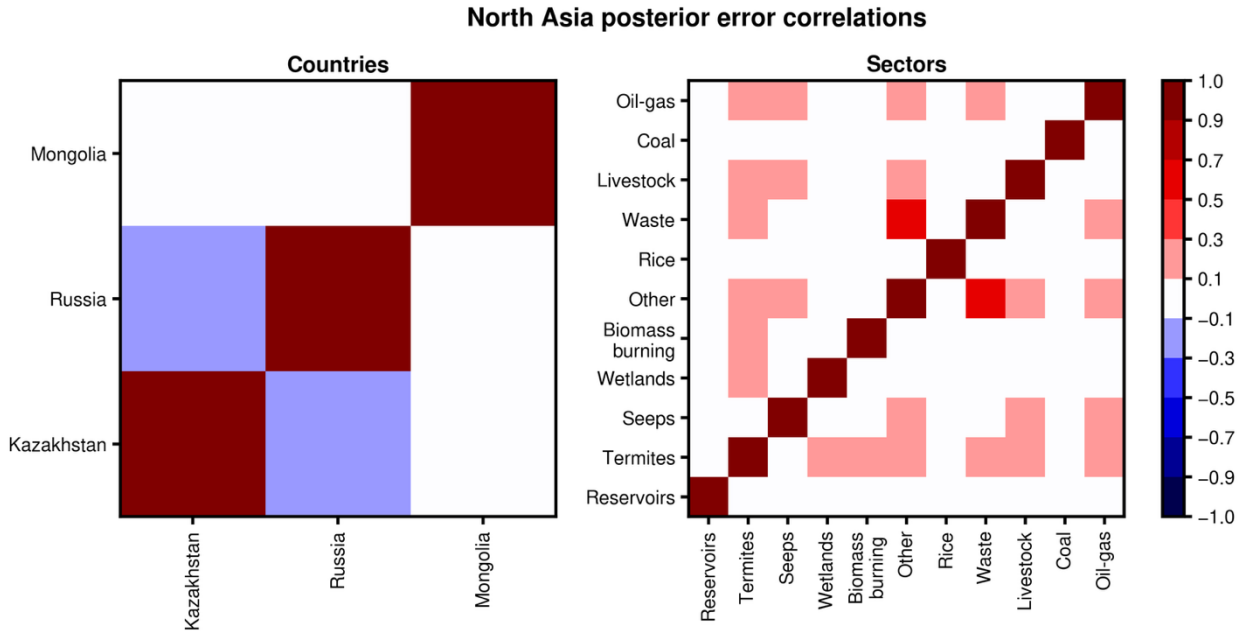

Fig. S8 | Posterior error correlations between individual countries and sectors in the North Asia. As in Fig. S3. Results are for region F in Fig. 1.

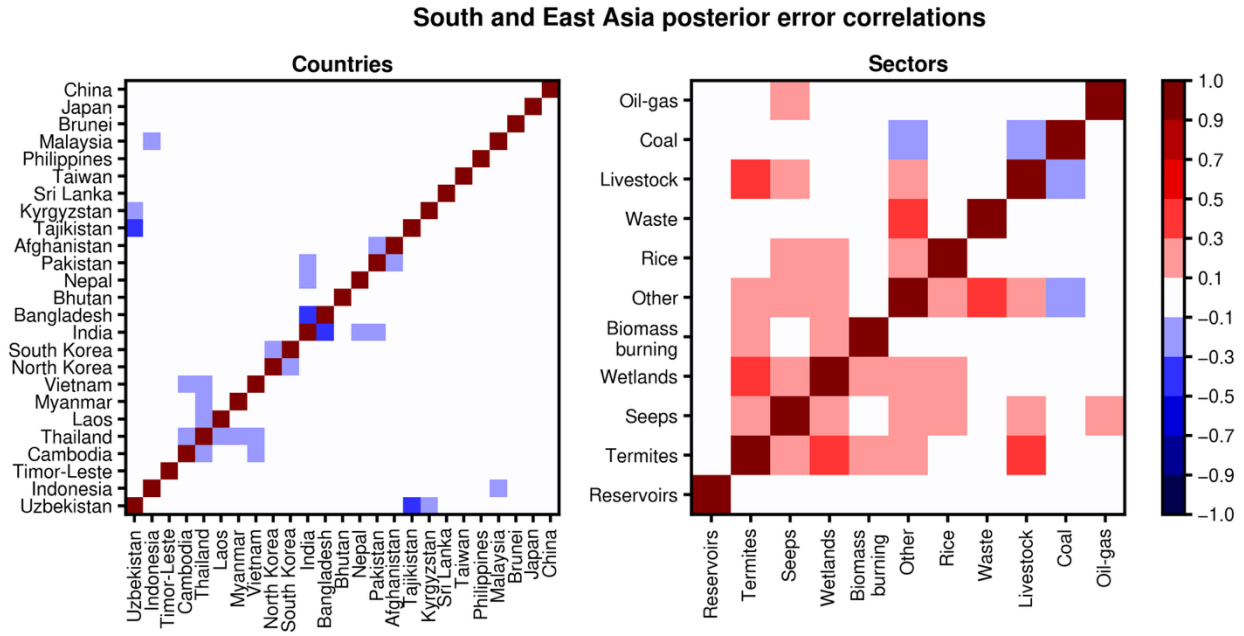

Fig. S9 | Posterior error correlations between individual countries and sectors in the South and East Asia. As in Fig. S3. Results are for region G in Fig. 1.

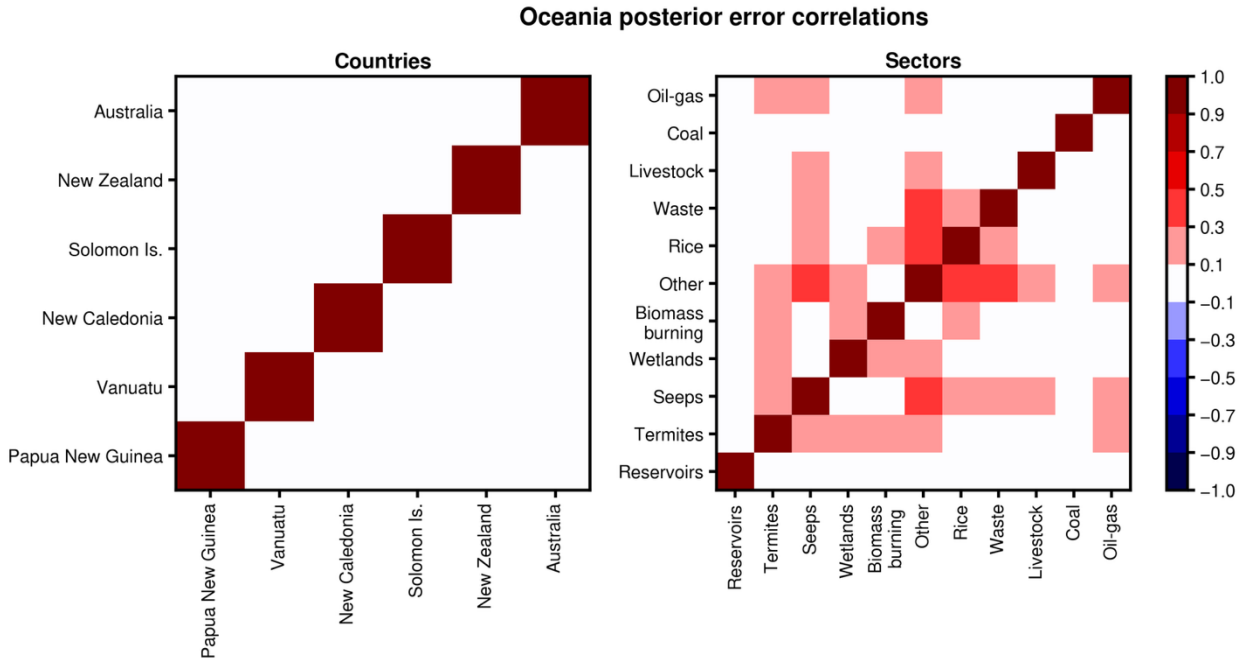

Fig. S10 | Posterior error correlations between individual countries and sectors in the Oceania. As in Fig. S3. Results are for region H in Fig. 1.

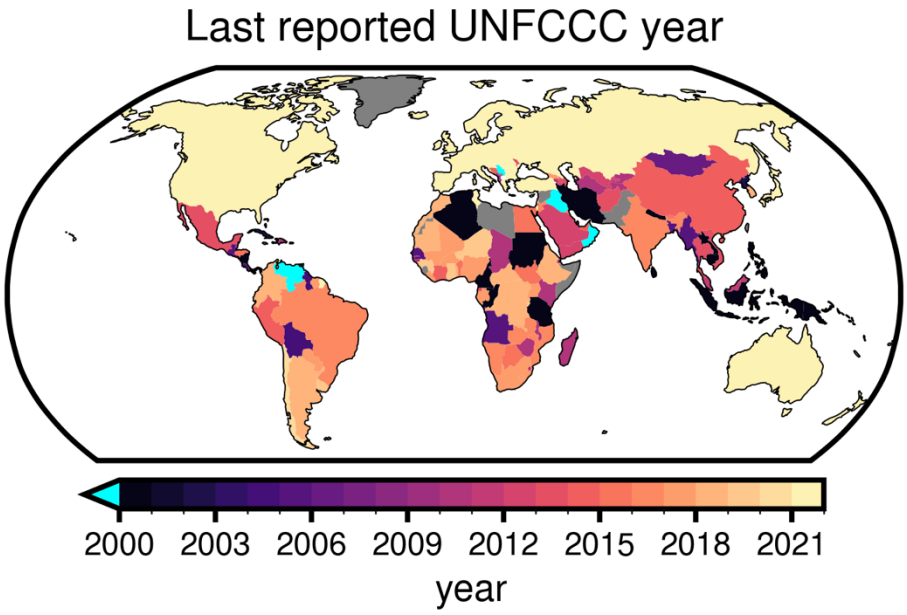

Fig. S11 | Year of UNFCCC report. Report year is also given in Table S1. Countries in grey do not report to UNFCCC. Most recent report year of countries in cyan is before 2000. Year of report is the tick mark on the left edge of the color boundary. Greenland's emissions are reported by Denmark.

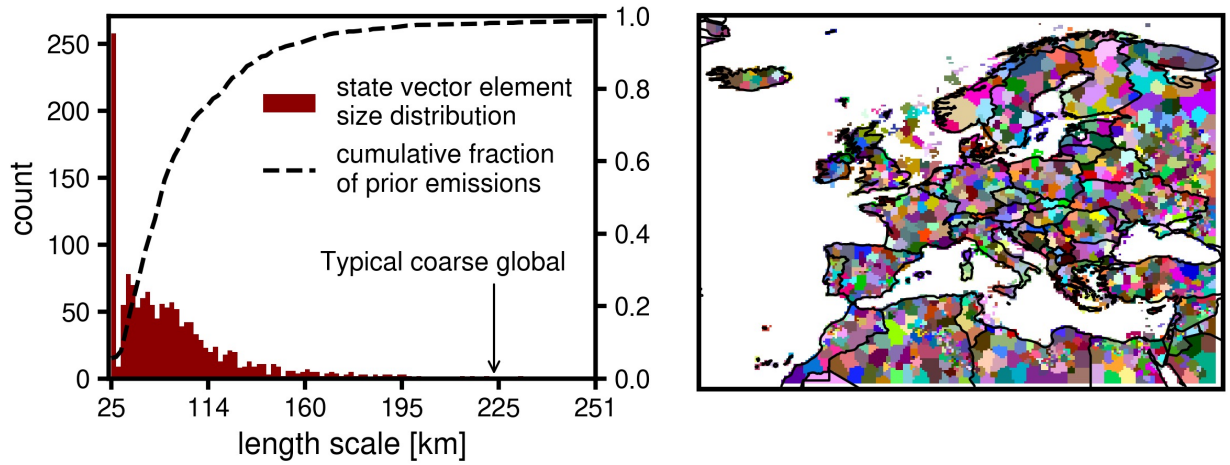

Fig. S12 | State vector size distribution and map. Europe and North Africa inversion region is shown as an example. (a) shows size distribution of state vector elements in terms length scale, where length scale is $\sqrt{(p25^2)}$ and p is the number of model grid cells in the state vector element. Also shown is the cumulative emissions fraction included in the state vector element, and the length scale of grid cell in a typical global inversion. (b) shows a map of the state vector, where the colors distinguish different state vector elements.

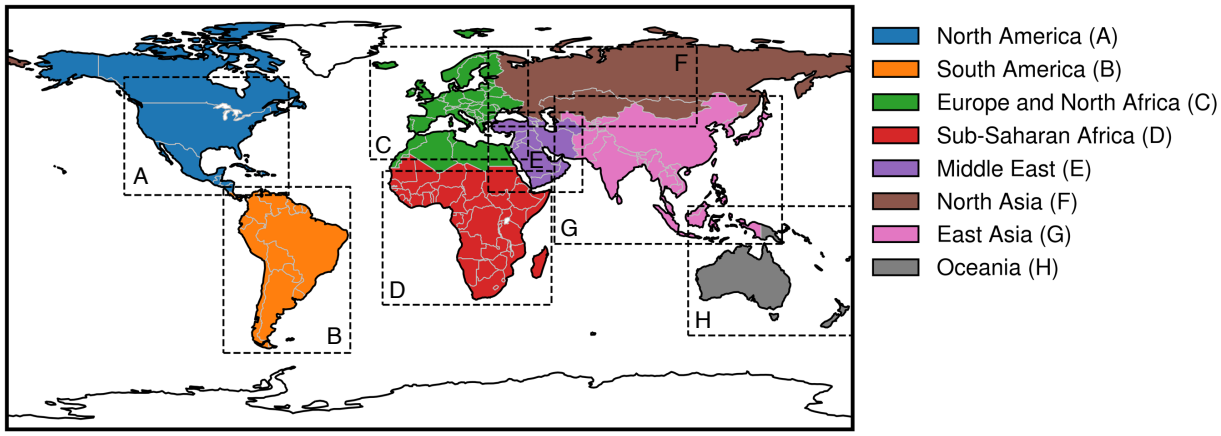

Fig. S13 | Map of inversion domains and target countries. Emissions in each country are optimized by a single inversion. The map shows which countries are optimized by which inversion domains. For locations where inversion domains overlap, posterior emissions from the primary domain only are used. For example, areas of Egypt are contained in inversion domains C and E. Egypt's inversion domain is Europe and North Africa (C), so the inversion results from that domain only are used in the posterior emissions.